Impacts of Assimilating Future Clear-Air Radial Velocity Observations from Phased Array Radar on Convection Initiation Forecasts: An Observing System Simulation Experiment Study⬦

Yongjie Huang,[a] Xuguang Wang,[a] Andrew Mahre,[a,b] Tian-You Yu,[a,b,c] and David Bodine[a,b]

[a] School of Meteorology, University of Oklahoma, Norman, Oklahoma
[b] Advanced Radar Research Center, University of Oklahoma, Norman, Oklahoma
[c] School of Electrical and Computer Engineering, University of Oklahoma, Norman, Oklahoma

ABSTRACT: Phased-array radar (PAR) technology can potentially provide high-quality clear-air radial velocity observations at a high spatiotemporal resolution, usually ∼1 min or less. These observations are hypothesized to partially fill the gaps in current operational observing systems with relatively coarse-resolution surface mesonet observations and the lack of high-resolution upper-air observations especially in planetary boundary layer. In this study, observing system simulation experiments are conducted to investigate the potential value of assimilating PAR observations of clear-air radial velocity to improve the forecast of convection initiation (CI) along small-scale boundary layer convergence zones. Both surface-based and elevated CIs driven by meso-γ-scale boundary layer convergence are tested. An ensemble Kalman filter method is used to assimilate synthetic surface mesonet observations and PAR clear-air radial velocity observations. Results show that assimilating only surface mesonet observations fails to predict either surface-based or elevated CI processes. Assimilating clear-air radial velocity observations in addition to surface mesonet observations can capture both surface-based and elevated CI processes successfully. Such an improvement benefits from the better analyses of boundary layer convergence, resulting from the assimilation of clear-air radial velocity observations. Additional improvement is observed with more frequent assimilation. Assimilating clear-air radial velocity observations only from the one radar results in analysis biases of cross-beam winds and CI location biases, and assimilating additional radial velocity observations from the second radar at an appropriate position can reduce these biases while sacrificing the CI timing. These results suggest the potential of assimilating clear-air radial velocity observations from PAR to improve the forecast of CI processes along boundary layer convergence zones.

KEYWORDS: Convective-scale processes; Radars/radar observations; Cloud-resolving models; Data assimilation

1. Introduction

Convection initiation (CI) commonly refers to the process that air parcels penetrate their level of free convection and buoyantly accelerate upward to generate a precipitating updraft, and form deep, moist convection (Markowski and Richardson 2010). To better understand and predict precisely when, where, and how deep convection initiates, several field campaigns have been conducted (Weckwerth et al. 2004; Browning et al. 2007; Geerts et al. 2017). The International H$_2$O Project (IHOP_2002) field campaign was conducted over the U.S. southern Great Plains with small local topographic variations from 13 May to 25 June 2002. One of its research components is CI (Weckwerth and Parsons 2006). There were total 112 CI cases during IHOP_2002. About one-half of these cases were triggered along surface-based convergence lines, and the other one-half were elevated initiation episodes with source air located at about 900–600 hPa. The surface-based cases occurred mostly during the afternoon and evening, and the elevated initiation episodes mostly occurred at night (Wilson and Roberts 2006). The Convective Storm Initiation Project (CSIP) field campaign was performed in southern coastal region of the United Kingdom during the summers of 2004 and 2005. During the CSIP field campaigns, almost all the convective storms were initiated in the planetary boundary layer (PBL), and only one case originated above the PBL (Browning et al. 2007). The Plains Elevated Convection at Night (PECAN) field campaign focused on nocturnal elevated convection over the U.S. central Great Plains in 2015. Improving the understanding and prediction of nocturnal CI is one of the primary scientific objectives of PECAN (Geerts et al. 2017; Weckwerth et al. 2019).

The triggering mechanisms for CI were better understood based on the results from the field campaigns (Wilson and Roberts 2006; Browning et al. 2007; Weckwerth et al. 2019) and many other previous studies (Koch and Clark 1999; Fovell 2005; Kang and Bryan 2011; Kirshbaum 2011; Lock and Houston 2014; Hill et al. 2016; Gasperoni et al. 2018; Degelia et al. 2018, 2019, 2020; Wang and Xue 2018; Huang et al. 2019; Parsons et al. 2019). Lock and Houston (2014) examined 55 000 CI cases and found that convergence and lift are the most significant parameters that effectively discriminate between initiation and non-initiation. A lower-tropospheric convergence mechanism for CI commonly includes frontal boundaries (e.g., Koch and Clark 1999), drylines (e.g., Hill et al. 2016; Gasperoni et al. 2018), sea-breeze fronts (e.g., Fovell

2005), cold pool gust fronts (e.g., Wilhelmson and Chen 1982; Huang et al. 2019), undular bores (e.g., Parsons et al. 2019), and horizontal convective rolls (e.g., Weckwerth 2000; Wang and Xue 2018), orographic circulations (e.g., Kirshbaum 2011), elevated convergence zones (e.g., Reif and Bluestein 2018; Weckwerth et al. 2019), and so on. The inhomogeneous heating of the underlying surface resulting in mesoscale circulations also can trigger CI (e.g., Kang and Bryan 2011).

A few studies have investigated the impact of assimilating different kinds of surface observations on the numerical prediction of CI (Sobash and Stensrud 2015; Madaus and Hakim 2017; Gasperoni et al. 2018; Degelia et al. 2018). Sobash and Stensrud (2015) revealed that assimilating high-frequency (every 5 min) mesonet surface observations in addition to conventional surface observations improved CI timing and location forecasts in a dryline case relative to the experiments that only assimilate conventional surface observations. The improvement was primarily due to the fact that the rapidly evolving mesoscale features are accurately captured by high-frequency mesonet data. Gasperoni et al. (2018) found that assimilating high spatiotemporal resolution nonconventional surface observations can capture the small-scale information in the dryline structures that cause localized enhanced convergence and correct the forecast of CI location in a dryline case. Madaus and Hakim (2017) used a series of observing system simulation experiments (OSSEs) to determine that assimilating at least 4-km-and especially 1-km-density surface observations can produce skillful and reliable *storm-scale* CI forecasts. Forecasts starting before cumulus formation lack CI forecast skill, however. Degelia et al. (2018) showed that CI was successfully forecast when assimilating in situ observations to strengthen low-level convergence and to enhance buoyancy.

Recently, some studies tried to explore the benefits of assimilating less-traditional upper-air observations to improve numerical prediction of CI (Keclik et al. 2017; Coniglio et al. 2019; Degelia et al. 2019, 2020). Assimilating temperature and dewpoint profiles retrieved from Atmospheric Emitted Radiance Interferometer (AERI) and horizontal wind profiles retrieved from Doppler lidar in addition to conventional observations can improve the short-term forecasts of the initiation and early evolution of thunderstorms (Coniglio et al. 2019). Degelia et al. (2019, 2020) determined that assimilating a mesoscale network of surface and profile observations collected during the PECAN field campaign can improve the forecasting of the timing and location of a CI event. However, Keclik et al. (2017) found that no statistically significant improvement in CI forecast skill was attained by assimilating meso-α- to synoptic-scale observations at mid- to upper troposphere collected during the 2013 Mesoscale Predictability Experiment (MPEX), likely because the lower-tropospheric environment modulating CI was not well captured by targeted observations.

Although the understanding and prediction of CI have been improved given the past efforts, challenges for CI prediction remain. CI is the result of the interactions among different scales including synoptic, meso-α, meso-β, meso-γ, and microscales (Keclik et al. 2017). Precise prediction of CI requires a numerical model to capture these multiscale interactions accurately, especially those interactions within PBL.

Additionally, Reif and Bluestein (2018) demonstrated that precise forecast of CI timing and location is especially challenging for highly localized events in the warm season. This challenge is partly due to the lack of high spatiotemporal resolution observations that are critical in sampling before and during CI.

Current operational observing systems lack high spatial (horizontal/vertical) and temporal resolution of atmospheric observations in the PBL (NRC 2009), which inhibits the improvement of CI forecasts. Although the National Weather Service (NWS) radiosonde network can provide high-quality vertical profiles of temperature, humidity and winds, it has a mean spacing of ~350 km and temporal resolution of 12 h. Mesoscale monitoring networks, such as the Oklahoma Mesonet, can provide observations at a spatial resolution of ~30–50 km every 5 min. However, these atmospheric observations are only near the surface and are still sparse for sampling many processes that affect localized CI. While satellite sensors generally can provide observations with relatively good horizontal and temporal coverage (Balsamo et al. 2018), their ability to sample the PBL is limited. Recent studies (e.g., Koch et al. 2018; Leuenberger et al. 2020) addressed the potential value of high spatial and temporal resolution PBL observations from ground-based remote sensing (e.g., lidar) systems and unmanned aerial vehicles (UAV) for forecasts of CI and thunderstorms. However, these observation systems lack operational maturity so far.

Currently, the Weather Surveillance Radar-1988 Doppler (WSR-88D) observations have been used successfully in convective-scale analysis and prediction due to their ability to sample convective storms at a high temporal and spatial resolution (Sun et al. 2014; Huang et al. 2020). However, WSR-88D data have limited utility before and during CI, because the radar is not sufficiently sensitive to capture available information especially in clear-air regions (Markowski et al. 2006; Huang et al. 2020). In contrast, the next generation phased-array radar (PAR) with the rapid and flexible scanning capability can potentially and partly fill this observational gap (Zrnić et al. 2007). PAR can sample the pre-CI environment using the high-sensitivity scanning mode and provide a full volume scan of clear-air radial velocity at a high spatial resolution and temporal resolution less than 1 min (Zrnić et al. 2019). Huang et al. (2020) indicated that assimilating PAR clear-air radial velocity observations can improve the forecasting of supercell intensity and track. Zrnić et al. (2007) proposed that assimilating these high spatiotemporal resolution data from clear-air boundary layer may improve the prediction of CI timing and location. As discussed earlier, current operational observing systems can relatively easily identify meso-β-scale (20–200 km) boundaries. However, CI typically occurs along only limited segments of such boundaries. The timing and location for such CI events are mainly associated with the meso-γ- (2–20 km) to microscale phenomena that determine local PBL lifting (Markowski et al. 2006; Keclik et al. 2017). Given the capability of its clear-air mode, the next generation PAR is expected to capture at least part of the meso-γ- to microscale features responsible for CI. In summary, the high spatiotemporal resolution volumetric PAR

clear-air radial velocity observations are expected to at least partly fill the gaps in the current operational observing systems. Such a gap-filling effect can potentially improve the predictability of both surface-based and elevated CI. To our knowledge, there are no peer-reviewed published research investigating the potential benefits of assimilating PAR clear-air data on CI forecasts. The primary goal of this study is to address the following scientific questions:

- What is the impact of assimilating future PAR-like clear-air radial velocity observations on surface-based CI prediction relative to the current surface mesonet observations?
- How can assimilating future PAR-like clear-air radial velocity observations impact the forecast of elevated CI?
- Do the benefits of assimilating PAR clear-air radial velocity observations on CI forecasts depend on the data assimilation (DA) frequency?

To answer these questions, a series of OSSEs with perfect-model assumption using two typical types of CI, surface-based and elevated CI cases, are designed and performed. The remainder of the paper is organized as follows. Section 2 describes the simulation configuration, simulated observations, and experiment design. Section 3 presents the results obtained from the experiments, and a summary is given in section 4.

2. Method

This study is an early study to examine the impact of assimilating PAR clear-air radial velocity observations on CI forecasts. OSSEs with the perfect-model assumption are conducted to explore the potential value of assimilating future PAR clear-air radial velocity observations to improve forecast of CI along the PBL convergence zones. Synthetic surface mesonet observations and PAR observations are generated by adding observation errors to the truth run. Idealized surface-based and elevated CI cases are designed separately with a perfect model assumption. These idealized OSSEs allow the understanding of the impacts of the PAR data for different mechanisms individually. Such an isolation will be difficult to achieve in the real model and real data experiments or OSSEs generated with the real numerical weather prediction (NWP) model where the simulated atmospheric systems are complicated and contain various mechanisms that are hard to separate. Similar perfect-model and idealized-case OSSEs were used in early published studies (e.g., Kong et al. 2018; Pan et al. 2018; Bachmann et al. 2019; Liu et al. 2019; Schröttle et al. 2020; Taylor et al. 2021; Zhao et al. 2021).

a. Nature run

The truth or nature run is created using the Weather Research and Forecasting (WRF) Model, version 3.4.1, with the idealized run configuration. The quarter-circle hodograph environmental sounding used in Huang et al. (2020) is adopted for the homogeneous initial condition in the truth run. Open boundary conditions in both x and y directions are used for the lateral boundary condition of the truth run. The model domain is 200 km $\times$ 200 km with 1-km horizontal grid

spacing. A stretched grid is adopted in the vertical direction with an averaged vertical grid spacing of 500 m and a model top at 20-km height. The physics parameterizations used in truth run include MM5 Monin–Obukhov surface-layer scheme (Jiménez et al. 2012) and Thompson microphysics scheme with five cloud species (Thompson et al. 2008). A 1.5-order turbulent kinetic energy (TKE) closure scheme (Skamarock et al. 2008) is used to calculate the horizontal and vertical subgrid-scale mixing. Longwave radiation, shortwave radiation, land surface, PBL, and cumulus schemes are not activated.

A similar method to that described by Morrison et al. (2015) is adopted to initiate convection by applying forcing to v winds during the early integration. Convection is initiated by convergence at lower levels in the uniform thermodynamic environment. As discussed in the introduction, the current operational observing systems, with relatively coarse resolution surface mesonet observations and the lack of high temporal and spatial resolution upper-air observations especially in planetary boundary layer, severely limit surface-based and elevated CI forecasting. The high spatiotemporal resolution volumetric PAR clear-air radial velocity observations can potentially fill the gaps. Meanwhile, projections of u, v, and w winds in the radar radial direction vary as a function of elevation angle. It is thus worth exploring whether assimilating radar radial velocity observations can capture the enhanced convergence zone, one critical mechanism for CI, at different height levels. Therefore, two cases, surface-based and elevated cases, with different maximum convergence layers will be investigated here. The forcing term added to v winds is prescribed as

$$
\frac{\partial v}{\partial t} = -\alpha \gamma \cos\left[\frac{\pi}{2}\sqrt{\left(\frac{x - x_c}{x_r}\right)^2 + \left(\frac{y - y_c}{y_r}\right)^2}\right] \\
\times \left\{\cosh\left[\frac{5(z - z_c)}{z_r}\right]\right\}^{-2}, \tag{1}
$$

where $\alpha = 0.05$ m s^{-2} is the maximum forcing amplitude; x and y are distances (km) perpendicular to the left and bottom domain edges, respectively; x_c and y_c are the horizontal location of the domain center; z is height (km); $z_c = 0$ and $z_c = 1.5$ km (referring to the height of maximum horizontal convergence shown in Fig. 6 in Weckwerth et al. 2019) for the surface-based case and elevated case, respectively; $x_r = y_r = z_r = 10$ km; and

$$
\gamma = \begin{cases} 1, & t \le 600 \\ 1 - (t - 600)/60, & 600 < t < 660, \\ 0, & t \ge 660 \end{cases} \tag{2}
$$

with t being time (s). Equation (2) means that the forcing term is added from $t = 0$ to 11 min. The forcing term is added to v winds only when $\{[(x - x_c)/x_r]^2 + [(y - y_c)/y_r]^2\}^{1/2} \le 1$, indicating that the convergence belongs to meso-γ scale.

The output data from the truth run at 1-min intervals are used to examine the CI process. In this study, CI is defined as

the first occurrence of composite radar reflectivity (CREF, the column maximum radar reflectivity) exceeding 35 dBZ, which is often used in previous studies (Trier et al. 2015; Gasperoni et al. 2018; Abulikemu et al. 2019). From the CREF evolution of the truth simulation (Fig. 1), the first CI for surface-based and elevated cases are at $t = 16$ and 20 min, respectively (Figs. 1a1,c1), followed by the convection. The spatial scale of both types of convection reaches ~20 km along the west–east axis at $t = 20$ and 30 min, respectively (Figs. 1a3,c3). From the cross sections of horizontal wind divergence, CI processes are associated with near-surface and upper-level horizontal convergence in surface-based and elevated CI cases, respectively (Figs. 1b1,d1), as designed in this study.

b. Synthetic observations

1) SIMULATED SURFACE MESONET OBSERVATIONS

The synthetic surface mesonet observations are generated from their corresponding fields of truth run. There are five surface observation types including surface pressure, 10-m u wind, 10-m v wind, 2-m temperature, and 2-m specific humidity. The Oklahoma Mesonet can provide surface observation data at a spatial resolution of ~30–50 km and a temporal resolution of 5 min (McPherson et al. 2007). Thus, surface observations are simulated at 30-km horizontal spacing every 5 min. Following Madaus and Hakim (2017), observation errors of surface pressure, 10-m u/v winds, 2-m temperature, and 2-m specific humidity are drawn randomly from a Gaussian distribution with a zero mean and a standard deviation of 1 hPa, 1 m s^{-1}, 1 K, and 1 g kg^{-1}, respectively. This design ensures that the observation innovations (observation minus model states mapped to the observation locations) are not zero for surface mesonet observations.

2) SIMULATED PAR RADIAL VELOCITY OBSERVATIONS

Two assumed radars are located to ~25 km south and east of the domain center, respectively (Fig. 1). Such a placement of radars is based on the following justification. To assure the accuracy of derived winds, clear-air radar echoes from particulates (e.g., insects) or from refractive index turbulence observed in the vicinity of radar (within 50-km range) are often used (Wilson et al. 1994; Kollias et al. 2018). A single radar only observes winds in the radial direction and therefore cannot measure cross-beam winds. With the largest elevation angle of 19.5° in this study, radial wind represents mainly horizontal winds and limited w wind (Lippi et al. 2019). The south radar is mainly used to capture more v component of horizontal winds, and the east one is mainly used to capture more u component of horizontal winds. Two closely located PARs seem to be unlikely for the future PAR network due to the high cost. However, it is still worth examining the effects of the viewing angle geometry. It should be noted that this study is the first to explore the potential benefit of assimilating PAR clear-air radial velocity observations to CI forecasts. Therefore, the goal is to offer a proof of concept rather than to inclusively examine the sensitivity of all radar locations. The synthetic PAR radial velocity observations are

generated every 1 min using 360° azimuth scan. Each volume scan consists of 14 predefined elevation angles, that is, 0.5°, 1.5°, 2.4°, 3.4°, 4.3°, 5.3°, 6.2°, 7.5°, 8.7°, 10.0°, 12.0°, 14.0°, 16.7°, and 19.5°, which is the WSR-88D predefined Volume Coverage Pattern 11 (VCP 11). Xu et al. (2008) indicated that assimilation performance and model forecasts are not improved by making spatial resolution of radar observations higher than the model resolution. Therefore, in this study observations on each tilt are interpolated to the model horizontal grid locations for assimilation, same as Pan et al. (2018). That is radar observations are on the model grid location in the horizontal direction and on the radar tilt in the vertical direction. The highest-allowed observation height for clear-air radial velocity is 7 km above ground level (AGL) (Zrnić et al. 2019). There are ~210 000 PAR radial velocity observations for each radar assimilated in each DA cycle.

For the observation error of radial velocity, Dowell et al. (2004) used an observation error standard deviation of 2 m s^{-1} in their study, which has been widely used in the radar DA community (e.g., Yussouf et al. 2013; Johnson et al. 2015; Wang and Wang 2017). Dowell et al. (2004) found that using observation error standard deviations of either 3 or 4 m s^{-1} did not worsen the verification scores significantly. In this study, the observation error variance of PAR radial velocity is estimated using the method described in Yu et al. (2007). The mean velocity estimator variance (Yu et al. 2007) is

$$\mathrm{var}(\hat{v}_C) = \frac{K}{M-1}\left\{[1 - \rho^2(T_s)]\sum_{l=-(M-2)}^{M-2}\frac{M-1-|l|}{M-1}\rho^2(lT_s)\right.$$
$$\left. + \frac{1}{\mathrm{SNR}^2} + \frac{1}{\mathrm{SNR}}\left[1 - \frac{M-2}{M-1}\rho(2T_s)\right]\right\}, \quad (3)$$

where $\mathrm{var}(\hat{v}_C)$ is the variance of mean velocity estimator, M is the sample number, T_s is pulse repetition time (PRT), $\rho()$ is the normalized correlation coefficient of weather signals as a function of PRT, SNR is the signal-to-noise ratio, and $K = \lambda^2/[32\pi^2 T_s^2 \rho^2(T_s)]$, with λ being the radar wavelength. In Huang et al. (2020), an observation error standard deviation of 4 m s^{-1} is used for clear-air radial velocity observations based on Eq. (3). This error estimate is believed to be a high-end estimate, consistent for a scenario of a long PRT for multifunction radar where only a portion of the scan timeline is devoted to weather observations. In this paper, an observation error standard deviation of 2 m s^{-1} is used, which is more consistent with a "middle-of-the-road" estimate. In such scenario, a shorter PRT is used. PAR is mostly (or entirely) used for weather observations, and signal processing techniques such as beam multiplexing are used to achieve better data quality (Mahre et al. 2020). Note that sensitivity experiments using observation error standard deviation of 4 m s^{-1} were conducted, and the verification scores did not worsen especially in the elevated CI case.

c. Experiment design

A 50-member ensemble with a perfect model assumption is generated for OSSEs. Initial ensemble diversity is created by
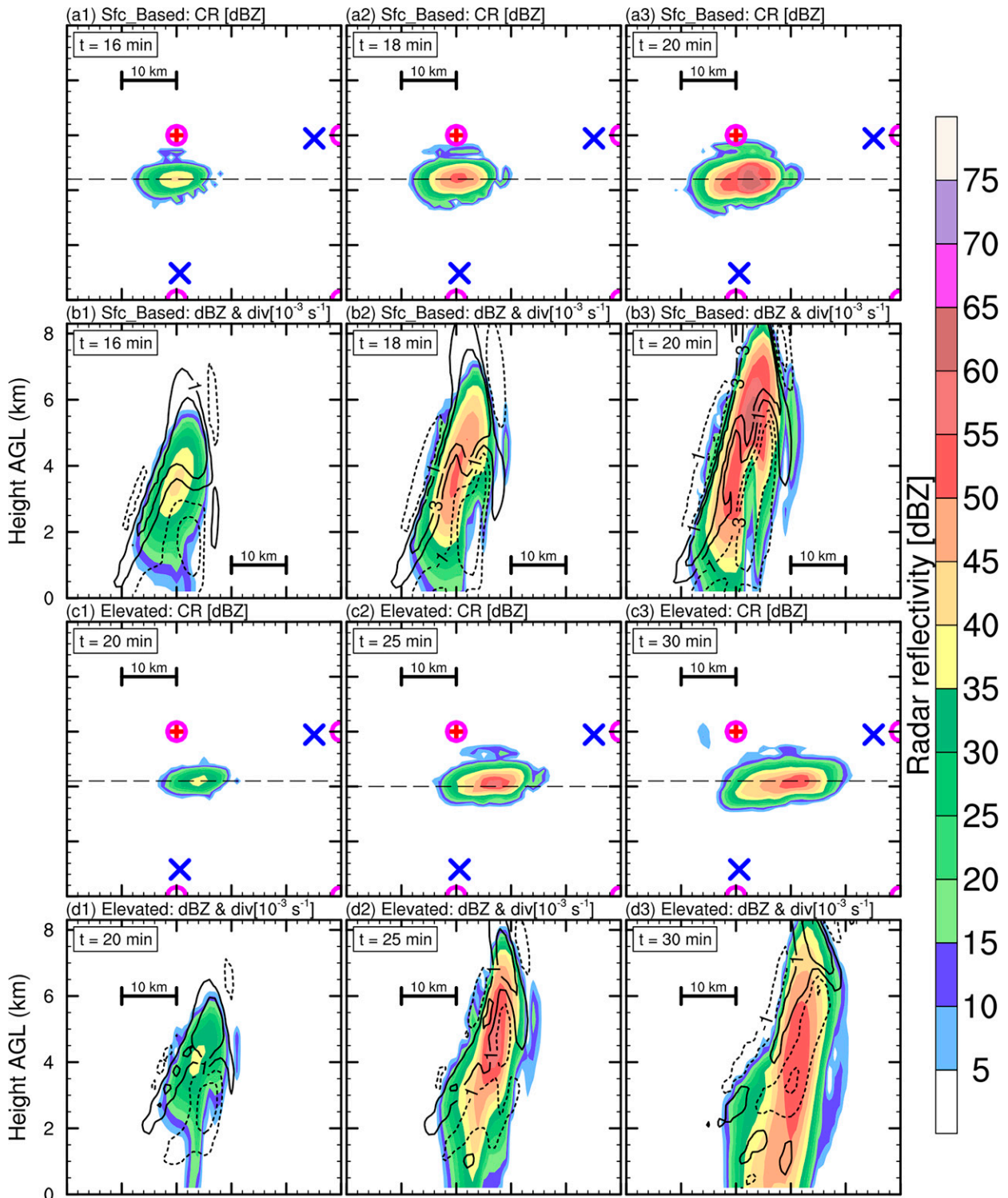
FIG. 1. Composite radar reflectivity (shaded) of the truth simulation for (a1)–(a3) surface-based case from $t = 16$ to 20 min in 2-min intervals and for (c1)–(c3) elevated case from $t = 20$ to 30 min in 5-min intervals. Also shown are height–x cross sections of radar reflectivity (shaded) and horizontal wind divergence ($\partial u/\partial x + \partial v/\partial y$; black contours $= -3, -1, 1$, and 3×10^{-3} s^{-1}, with dashed contours being negative values) along the dashed lines shown in (a1)–(a3) and (c1)–(c3) in the truth simulation for (b1)–(b3) surface-based and (d1)–(d3) elevated cases. The red plus sign indicates the center of the model domain, the magenta circles denote the locations of surface mesonet observations, and the blue times signs indicate the locations of the radar in the south and east. Minor tick marks are included every 2 km, and major tick marks are included every 10 km.
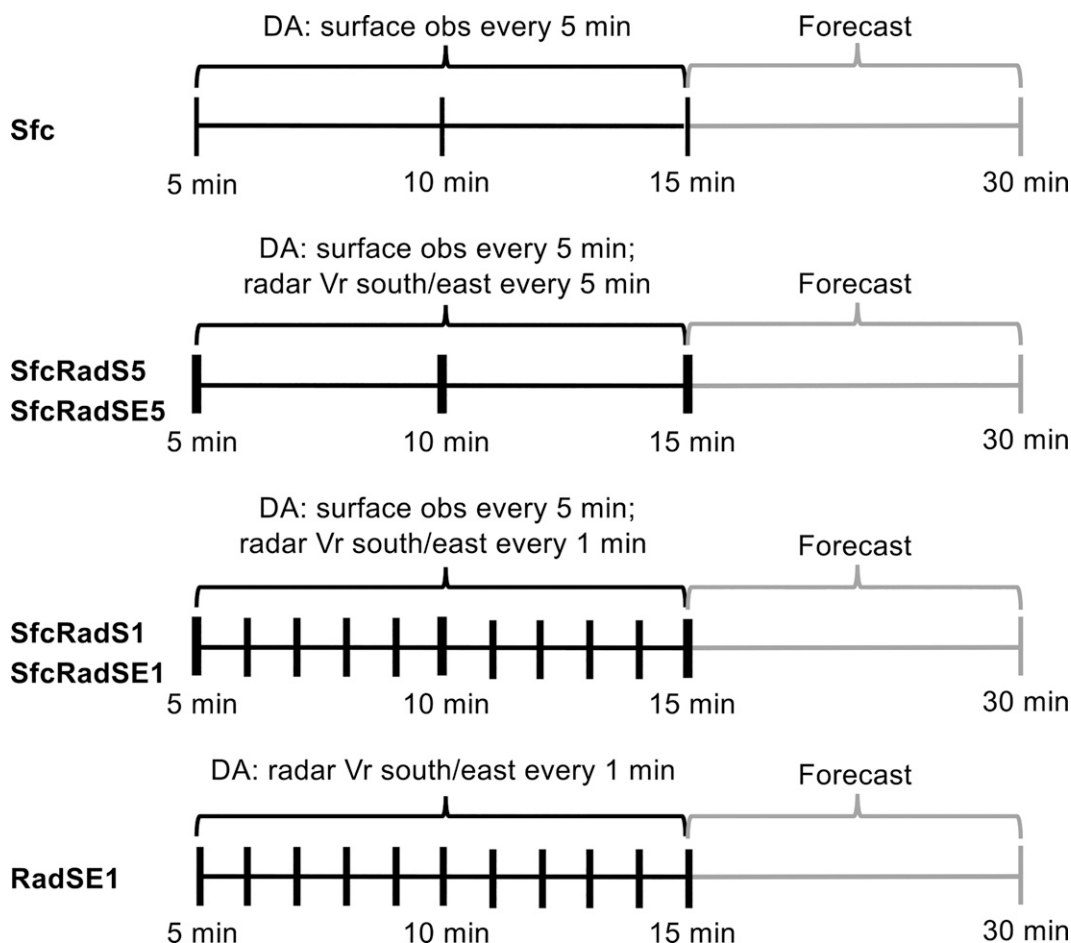
FIG. 2. Timelines of the DA experiments assimilating observations from $t = 5$ to 15 min (10-min DA period). The model forecasts go from the end of the DA windows ($t = 15$ min) to $t = 30$ min. See the text for details.

perturbing u and v wind fields using uncorrelated Gaussian perturbation from the surface up to 11 km height at the initial time. The standard deviation of the perturbations is 4 m s^{-1} from the surface up to 11 km height and linearly decreasing to 0 m s^{-1} at the 13 km height, which is the same as Huang et al. (2020). There are therefore also differences between the truth simulation and the ensembles outside of the region of perturbed v winds.

An ensemble adjustment Kalman filter (Anderson 2001) from the Data Assimilation Research Testbed (DART; https://dart. ucar.edu; Anderson et al. 2009) is adopted for DA. Horizontal and vertical spatial covariance localization (Gaspari and Cohn 1999) with a 60- and 3-km cutoff radius, respectively, are used for surface observations (Sobash and Stensrud 2015), and with 6- and 3-km cutoff radius, respectively, for PAR radial velocity observations (Dowell et al. 2011). Meanwhile, to counteract the spread values decreasing tendency during assimilation update, an adaptive prior inflation (Anderson 2009) is used. The initial values to set for the inflation and inflation standard deviation are 1.0 and 0.8, respectively. The lower bounds of the inflation and inflation standard deviation are set to 1 and 0.8, respectively. The inflation damping is set to a value of 0.9. The variables updated by the DA include three components of wind (u, v,

and w), geopotential height, potential temperature, pressure, and mixing ratio of water species.

The control experiment (CRTL) conducts no DA and applies the forcing term of Eq. (1) to the v wind and coefficient γ based on Eq. (2) starting from $t = 5$ to 11 min because of the perfect model assumption. To explore the potential value of assimilating PAR clear-air radial velocity observations to CI forecasts, six additional experiments are performed in addition to CTRL. The timelines for these six experiments are shown in Fig. 2. The experiment marked as Sfc is the same as CTRL except that surface observations are assimilated every 5 min from $t = 5$ to 15 min. The experiments SfcRadS5 and SfcRadSE5 are the same as Sfc except that additional radial velocity observations respectively from the southern radar only and both the southern and eastern radars are assimilated every 5 min from $t = 5$ to 15 min. The experiments SfcRadS1 and SfcRadSE1 are the same as SfcRadS5 and SfcRadSE5, respectively, except that radial velocity observations are assimilated every 1 min from $t = 5$ to 15 min to investigate the benefits of assimilating high frequency radial velocity data. To further review the impact of PAR clear-air radial velocity assimilation, the final experiment

RadSE1 is conducted. RadSE1 is the same as SfcRadSE1, except that no surface observations are assimilated in RadSE1. The free forecasts in all the experiments are started from $t = 15$ to 30 min. Through comparing the observation-space root-mean-square innovation and total ensemble spread (standard deviation) for assimilated radial velocity observations in both surface-based and elevated CI cases (Figs. S1 and S2 in the online supplemental material), in general, the consistency ratios (Dowell et al. 2004) of ~1.04 in the experiments assimilating radial velocity every 1 min are close to the perfect value of 1. The ensembles in the experiments assimilating radial velocity every 5 min are slightly overdispersive with a consistency ratio of ~1.12, which is within the range of similar radar DA studies (e.g., Dowell et al. 2004; Yussouf et al. 2013; Huang et al. 2020).

d. Extended fractions skill score

The extended fractions skill score (FSS) (Duc et al. 2013) is adopted to evaluate the forecast skill of the ensemble forecasts. The extended FSS is an extension of the original neighborhood verification method (FSS; Roberts and Lean 2008) with the ensemble dimension included. To attain extended FSS, the observed and forecast fraction of each neighborhood grid box P_f and P_o are computed first:

$$P_o(i,j) = \frac{1}{n^2} \sum_{ii=i-n/2}^{i+n/2} \sum_{jj=j-n/2}^{j+n/2} I_o(ii,jj) \quad \text{and} \quad (4)$$

$$P_f(i,j) = \frac{1}{n^2 m} \sum_{ii=i-n/2}^{i+n/2} \sum_{jj=j-n/2}^{j+n/2} \sum_{kk=1}^{m} I_f(ii,jj,kk), \quad (5)$$

where n is the size of square-shaped neighborhood and m is the number of ensemble members ($m = 50$ in this study). Here, I_o and I_f are binary variables with their values of 1 corresponding to events being observed and forecast, respectively, and 0 otherwise. A CREF threshold of 35 dBZ is used to calculate I_o and I_f. A square-shaped neighborhood with a width of 8 times horizontal grid spacing (4-km side half-length; Huang et al. 2020) is considered. Then, the extended FSS is given by

$$FSS = 1 - \frac{\frac{1}{N_x N_y} \sum_{i=1}^{N_x} \sum_{j=1}^{N_y} [P_f(ij) - P_o(i,j)]^2}{\frac{1}{N_x N_y} \sum_{i=1}^{N_x} \sum_{j=1}^{N_y} [P_f^2(i,j) + P_o^2(i,j)]}, \quad (6)$$

where N_x and N_y are the number of grid points in the x and y axis in the examined domain, respectively. The FSS range is between 0 and 1, with no forecast skill when FSS = 0 and perfect forecast when FSS = 1.

3. Results

a. Surface-based CI case

1) FORECAST SKILL EVALUATION

Figure 3 shows the extended FSS of ensemble forecasts from $t = 15$ to 30 min in 1-min intervals for the surface-based
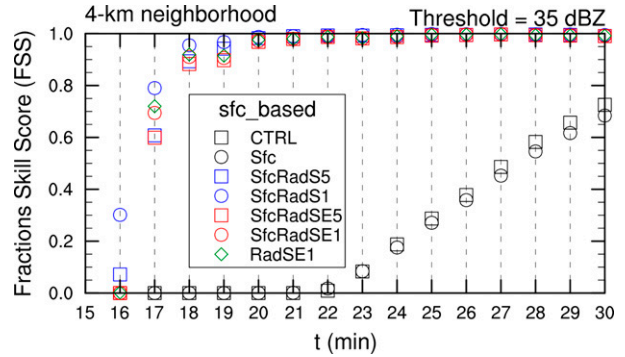

FIG. 3. Extended FSSs of CTRL, Sfc, SfcRadS5, SfcRadS1, SfcRadSE5, SfcRadSE1, and RadSE1 ensemble forecasts from $t = 15$ to 30 min in 1-min intervals for the surface-based CI case.

CI case. CTRL and Sfc do not have grid points indicating CI (i.e., FSS > 0) until $t = 22$ min, which is 6 min later than the truth simulation ($t = 16$ min). Their FSSs are very close and reach ~0.7 at $t = 30$ min. This result indicates assimilating surface mesonet observations alone has little impact on the simulated CI process. Starting from $t = 17$ min, all experiments assimilating clear-air radial velocity observations have higher FSSs than CTRL and Sfc. They all have almost perfect forecasts with FSS = ~1 starting $t = 20$ min. Therefore, assimilating clear-air radial velocity observations can significantly improve the CI forecast in this surface-based case. After assimilating the clear-air radial velocity observations from the southern radar, both SfcRadS5 (FSS = ~0.075) and SfcRadS1 (FSS = ~0.3) have captured CI grid points with the same CI timing as the truth simulation ($t = 16$ min). At $t = 17$ min, both SfcRadS5 and SfcRadS1 have high CI forecast skills with FSSs not less than 0.6, especially SfcRadS1 with FSS = ~0.8. Before $t = 20$ min, SfcRadS1 has higher FSSs than SfcRadS5 and SfcRadSE1 has higher FSSs than SfcRadSE5, indicating assimilating higher time-frequency clear-air radial velocity observations can attain higher FSSs in this surface-based case. With an additional radar, SfcRadSE1 and SfcRadSE5 do not perform significantly better than experiments using one southern radar (SfcRadS1 and SfcRadS5). The differences in dynamic fields will be examined in later sections to understand the differences in FSSs among these experiments. The similar forecast skills between SfcRadSE1 and RadSE1 further confirm the little impact of assimilating surface mesonet observations.

2) PROBABILISTIC FORECASTS OF CONVECTION INITIATION

The probability of CREF ≥ 35 dBZ in the ensemble forecasts of the surface-based case from $t = 16$ to 20 min in 1-min intervals is shown in Fig. 4. No members of Sfc and CTRL ensemble forecasts can capture the CI process, evidenced by the probability forecast of 0 from $t = 16$ to 20 min (Figs. 4a2–e2) consistent with FSS = 0 (Fig. 3). The other experiments assimilating PAR clear-air radial velocity data all begin to capture the CI process from $t = 17$ min and beyond
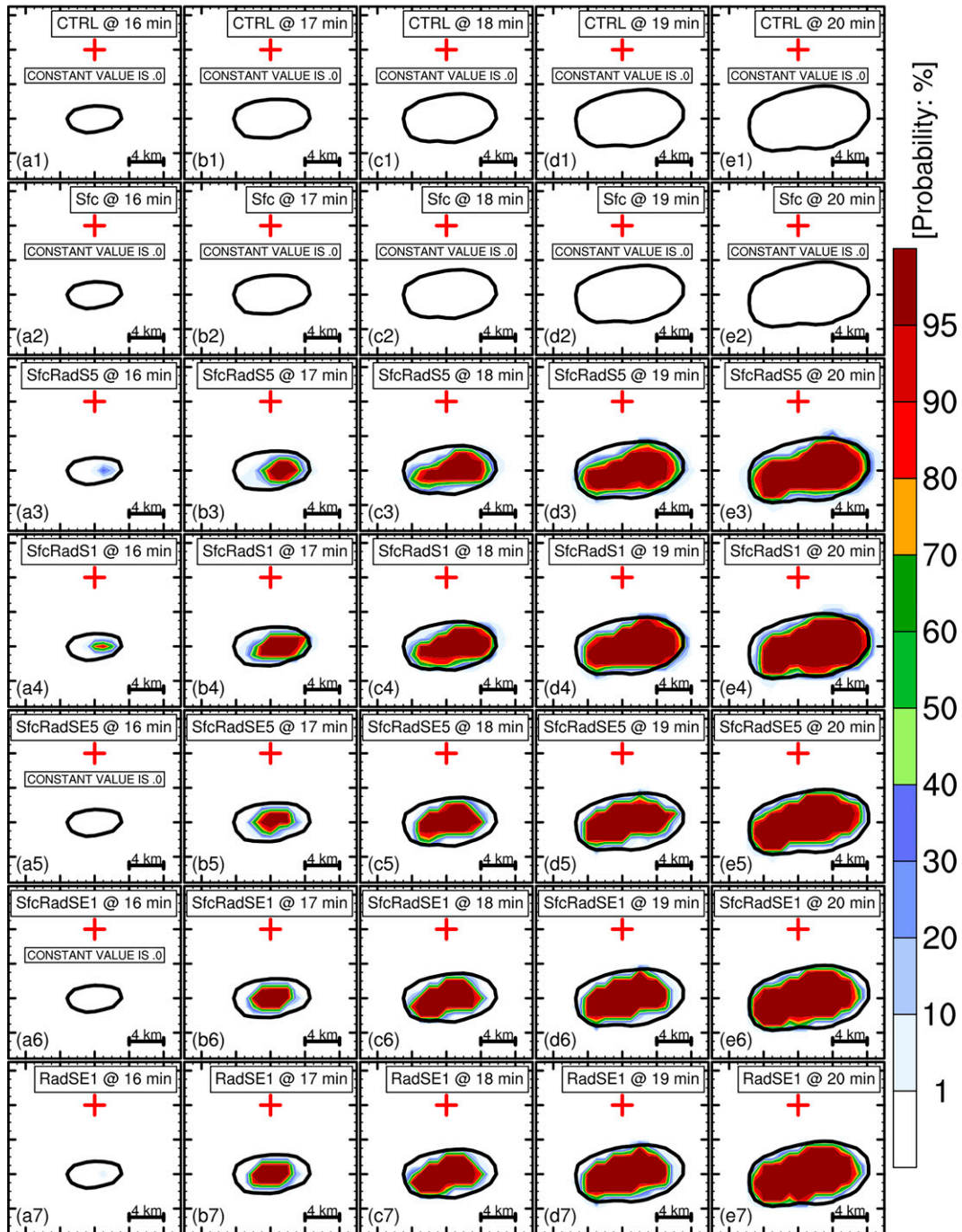
Surface-based Case

FIG. 4. Probability (shaded; %) of CREF ≥ 35 dBZ in the ensemble forecasts (a1)–(e1) CTRL, (a2)–(e2) Sfc, (a3)–(e3) SfcRadS5, (a4)–(e4) SfcRadS1, (a5)–(e5) SfcRadSE5, (a6)–(e6) SfcRadSE1, and (a7)–(e7) RadSE1 from $t = 16$ to 20 min in 1-min intervals. The black contours represent the CREF = 35 dBZ in the truth simulation. The red plus signs indicate the center of the model domain. Minor tick marks are included every 1 km, and major tick marks are included every 4 km.

(Figs. 4a3–e7). Some members of SfcRadS5, SfcRadS1 and RadSE1 are able to predict CI even earlier at $t = 16$ min, the same CI onset time as in the truth. SfcRadS1 performs the best in capturing the CI at $t = 16$ min with a greater probability

(Figs. 4a3,a4,a7). Beginning at $t = 19$ min, the probability over 95% cover almost the entire swaths of CREF ≥ 35 dBZ of the truth simulation for all experiments assimilating PAR clear-air observations. The length of this swath's west–east

axis is ~14 km at t = 20 min, belonging to meso-γ scale. Therefore, assimilating clear-air radial velocity observations can significantly improve the meso-γ-scale CI forecast in this surface-based case.

From the probability difference between SfcRadS1 and SfcRadS5 (Figs. 5a1–d1), SfcRadS1 has larger probability in most areas within the truth swath of CREF ≥ 35 dBZ, indicating more frequently assimilating clear-air radial velocity observations from the southern radar can improve the CI forecast in this surface-based case. This result is consistent with the higher FSSs in SfcRadS1. The slight eastward location bias in SfcRadS1 leads to some negative and positive values of probability difference, respectively, within and outside the true swath of CREF ≥ 35 dBZ from t = 18 to 20 min (Figs. 5b1–d1). From the difference between SfcRadSE1 and SfcRadSE5 (Figs. 5a2–d2), similarly most areas have a positive impact of assimilating higher frequency clear-air radial velocity observations on CI forecast. Assimilating additional clear-air radial velocity observations from the eastern radar (SfcRadSE1) can correct the eastward location bias of SfcRadS1 (Figs. 5a3–d3). From the difference between SfcRadSE1 and RadSE1 (Figs. 5a4–d4), assimilating surface mesonet observations slightly reduces the probability within the swath of CREF ≥ 35 dBZ in the truth simulation. This result suggests the surface observation simulated at the current mesonet spacing is not helpful in capturing the surface meso-γ-scale convergence likely due to its coarse resolution.

3) WIND AND CONVERGENCE FIELDS

To investigate the impacts of assimilating clear-air radial velocity observations and the differences among various experiments, dynamic fields including three-dimensional winds and horizontal convergence are examined and diagnosed.

At the end of the final DA cycle (t = 15 min), vertical velocities are over 2.4 and 10 m s^{-1} at 0.5 and 3.5 km AGL, respectively, in the truth simulation (Figs. 6a1,b1). Northerly horizontal winds at 0.5 km AGL (Fig. 6a1) and divergent horizontal winds near the strong vertical velocity center (Fig. 6b1) with the divergence over 3 × 10^{-3} s^{-1} at 3.5 km AGL (Fig. 7a) dominate the truth simulation. The maximum vertical velocity within the model volume in the truth simulation is 10.7 m s^{-1}, and the convergence below the strong vertical motion center and divergence above the strong vertical motion center both exceeds 3 × 10^{-3} s^{-1} (Fig. 7a).

CTRL contains maximum absolute errors of horizontal velocity, vertical velocity, and horizontal divergence over 9.5, 1.9 m s^{-1}, and 1 × 10^{-3} at 0.5 km AGL and over 9.1, 10 m s^{-1}, and 3 × 10^{-3} s^{-1} at 3.5 km AGL, respectively (Figs. 6a2,b2 and 7b). Maximum absolute errors of both horizontal convergence and divergence in CTRL are over 3 × 10^{-3} s^{-1} in the lower and upper levels, and maximum vertical velocity within the model volume is 1.5 m s^{-1} and is weaker than the truth. Assimilating only surface mesonet observations (Sfc) has little impact on correcting these errors (Figs. 6a3,b3 and 7b). After assimilating additional clear-air radial velocity from the southern radar every 5 min (SfcRadS5), the winds are significantly improved with maximum absolute errors of vertical velocity

reduced to ~0.9 and ~4.9 m s^{-1} at 0.5 and 3.5 km AGL, respectively (Figs. 6a4,b4). The maximum vertical velocity within the model volume in SfcRadS5 reaches 8.8 m s^{-1} (Figs. 6a4 and 7d), and the area coverage with absolute errors of divergence fields in SfcRadS5 over 1 × 10^{-3} s^{-1} is clearly reduced (Fig. 7d) relative to those in Sfc (Fig. 7c), which is consistent with the higher FSSs in SfcRadS5 (Fig. 3). Although the DA also updates the vertical velocity fields, the model's response to the DA dominates the vertical velocity evolution (not shown).

Relative to SfcRadS5 (Figs. 6a4), wind errors, especially u wind errors near the strong vertical motion center and domain center in SfcRadS1, are somewhat increased at 0.5 km AGL with maximum absolute errors of vertical velocity larger than 1 m s^{-1} (Fig. 6a5). Consistently, the areas with absolute divergence anomaly over 1 × 10^{-3} s^{-1} are slightly larger in SfcRadS1 than those in SfcRadS5 below 2 km AGL, and the errors in the x component of horizontal divergence are dominant (Fig. 7e). The wind fields at 3.5 km AGL in SfcRadS1 are slightly improved with smaller areas of absolute errors of vertical velocity over 4 m s^{-1} (Fig. 6b5). Diagnostics suggest that the ability of the ensemble to capture the covariance between radial velocity of the southern radar and u winds near strong updraft center is limited (not shown), resulting in large analysis errors of u winds in SfcRadS5 (Figs. 6a4 and 7d). This is expected based on the radar viewing geometry where v winds are aligned more closely to the radar beam than u winds. These analysis errors increase with an increasing assimilation frequency as shown in SfcRadS1 (Figs. 6a5 and 7e). However, the larger analysis errors in divergence fields in the lower levels (Figs. 7d,e) result in vertical velocity aloft closer to the truth in the strong updraft center of the truth. This result is especially the case for SfcRadS1 with maximum vertical velocity of 10.8 m s^{-1} within the model volume. These results indicate that the improvement of SfcRadS1 relative to SfcRadS5 does not result from the more accurate analysis of meso-γ-scale horizontal convergence but from closer vertical updraft to the truth as a result of the larger u-wind biases.

After assimilating additional clear-air radial velocity from the eastern radar (SfcRadSE5 and SfcRadSE1), horizontal wind errors are reduced, particularly in the region near the strong vertical velocity center, relative to SfcRadS5 and SfcRadS1 (Figs. 6a4–a7,b4–b7). The improvement is also shown in divergence fields especially their x components in SfcRadSE5 and SfcRadSE1 (Figs. 7f,g). This result indicates that u winds can be corrected by assimilating clear-air radial velocity from additional radar located to the east of the storm, which is consistent with the smaller location biases in SfcRadSE5 and SfcRadSE1 (Fig. 5). When the radial velocity of the eastern radar is assimilated, v winds can be incremented. This increment is through ensemble covariance of the u and v winds. If such ensemble covariance is inaccurate or spurious, the v wind may be contaminated, which can result in enhanced v wind analysis errors in SfcRadSE5 and SfcRadSE1 (Figs. 6a6,a7 and 7f,g). Radial velocity from operational radars typically contains very limited contribution from w wind especially for low elevation angles near the
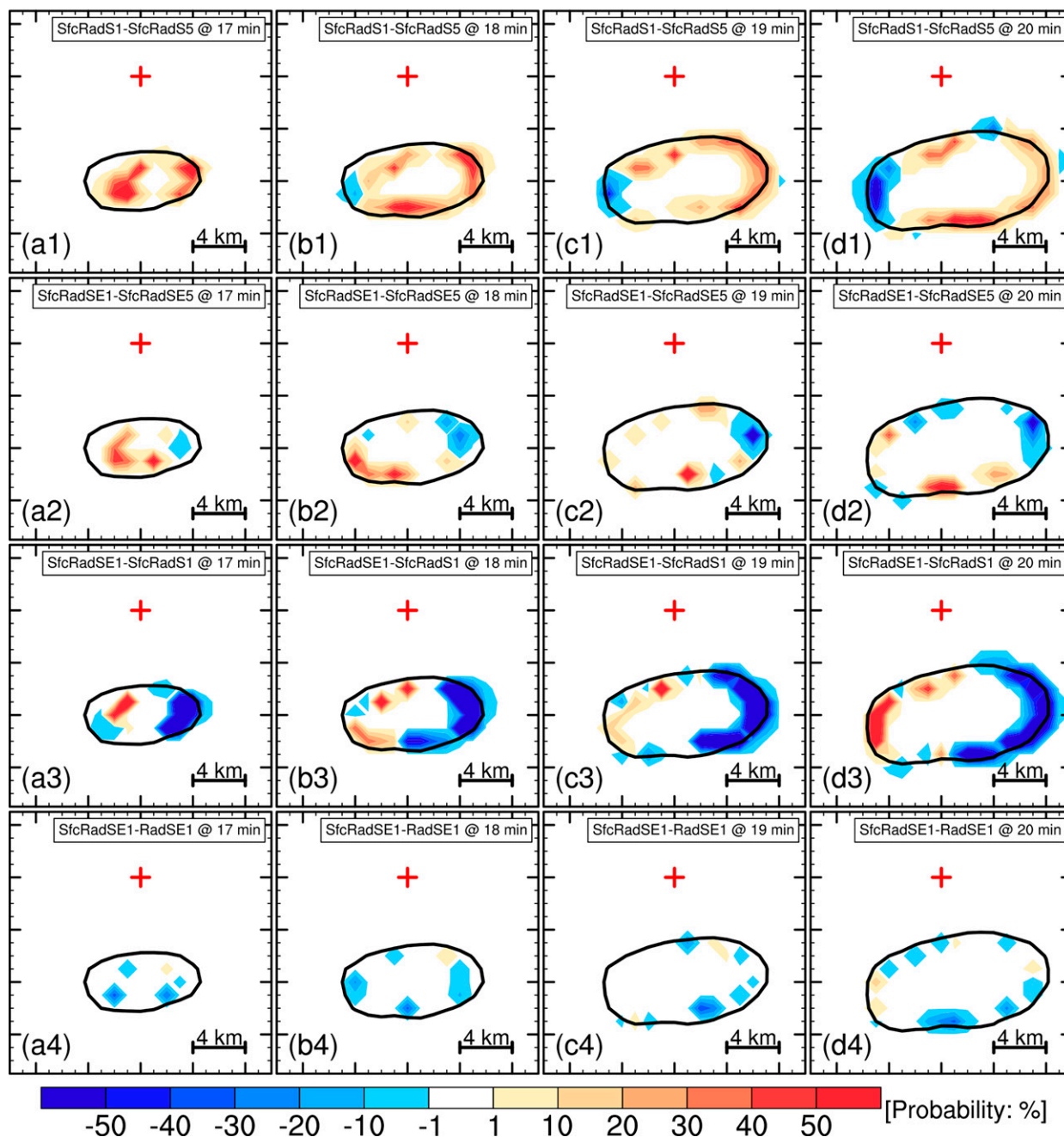
Surface-based Case

FIG. 5. Probability differences of CREF $\geq$ 35 dBZ (a1)–(d1) between SfcRadS1 and SfcRadS5, (a2)–(d2) between SfcRadSE1 and SfcRadSE5, (a3)–(d3) between SfcRadSE1 and SfcRadS1, and (a4)–(d4) between SfcRadSE1 and RadSE1 from $t = 17$ to 20 min in 1-min intervals. The black contours represent the CREF = 35 dBZ in the truth simulation. The red plus signs indicate the center of the model domain. Minor tick marks are included every 1 km, and major tick marks are included every 4 km.

surface. However, larger u-wind biases in SfcRadS5 and SfcRadS1 lead to stronger convergence in the lower levels and vertical updrafts in the updraft center of the truth than in SfcRadSE5 and SfcRadSE1, respectively (Figs. 6a4–a7,b4–b7), resulting in more accurate CI timing in SfcRadS5 and SfcRadS1 (Figs. 4a3–a6). Therefore, FSSs in SfcRadS5 and

SfcRadS1 are higher than those in SfcRadSE5 and SfcRadSE1 at the early stage of convection (Fig. 3). Meanwhile, SfcRadSE1 has a slightly better analysis than SfcRadSE5 in terms of wind and divergence fields, indicating the benefits of assimilating high frequency clear-air radial velocity observations from both radars. The small differences in
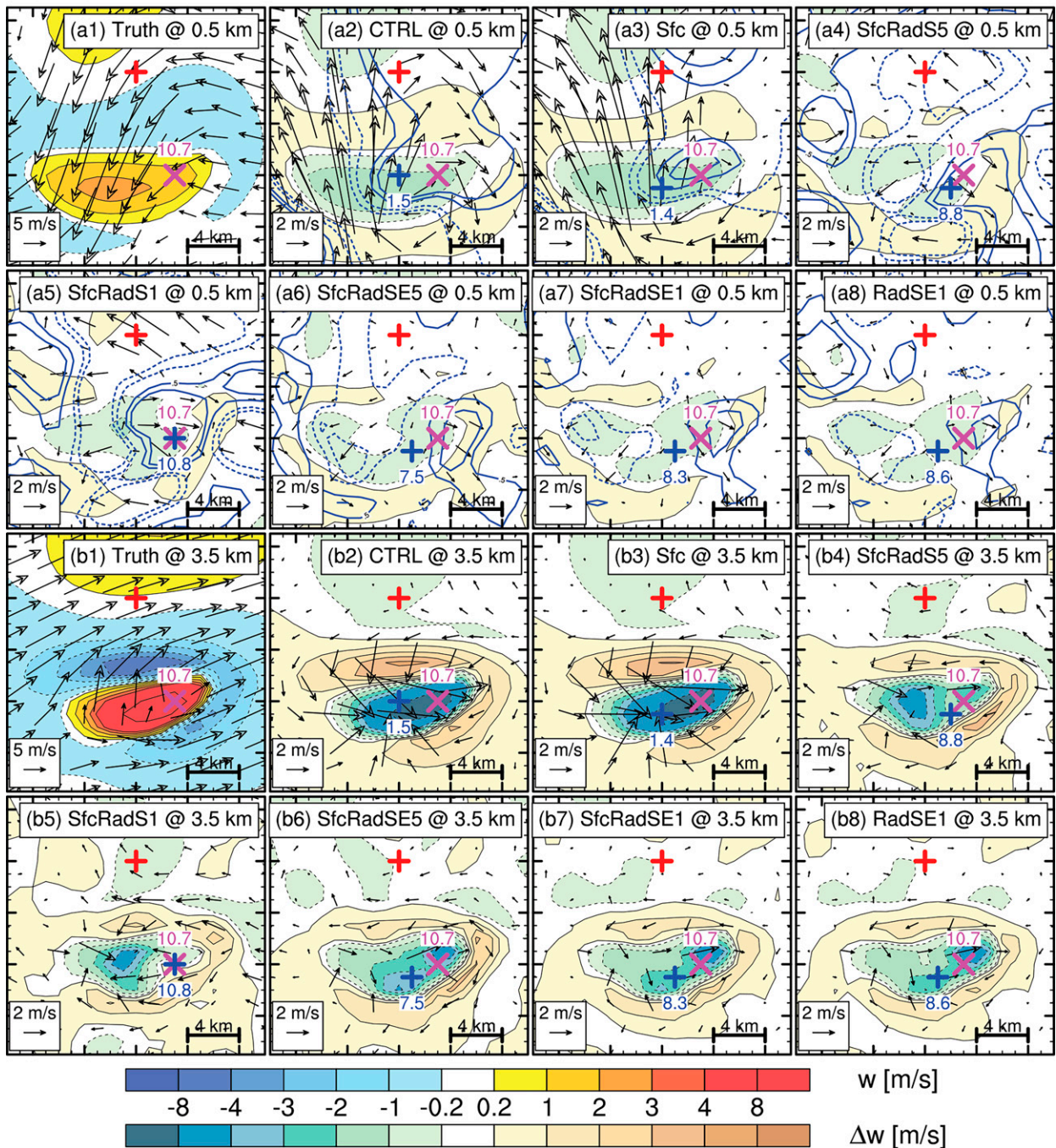
FIG. 6. Horizontal wind vectors and vertical velocity (shaded; m s^{-1}) in the truth simulation at (a1) 0.5 and (b1) 3.5 km AGL at $t = 15$ min. Also shown are the differences of horizontal wind vectors and vertical velocity (shaded; m s^{-1}) from the truth simulation for ensemble means of (a2),(b2) CTRL; (a3),(b3) Sfc; (a4),(b4) SfcRadS5; (a5),(b5) SfcRadS1; (a6),(b6) SfcRadSE5; (a7),(b7) SfcRadSE1; and (a8),(b8) RadSE1 at 0.5 [in (a2)–(a8)] and 3.5 [in (b2)–(b8)] km AGL. Blue contours in (a4)–(a8) indicate differences of u winds from the truth (contours $= -1$, -0.5, 0.5, and 1 m s^{-1}, with dashed contours being used for negative values). The red plus signs indicate the center of the model domain. The magenta times signs and blue plus signs represent the horizontal locations of maximum vertical velocity (corresponding color-coded figures) within the model volume in the truth simulation and sensitivity experiments, respectively. Minor tick marks are included every 1 km, and major tick marks are included every 4 km.
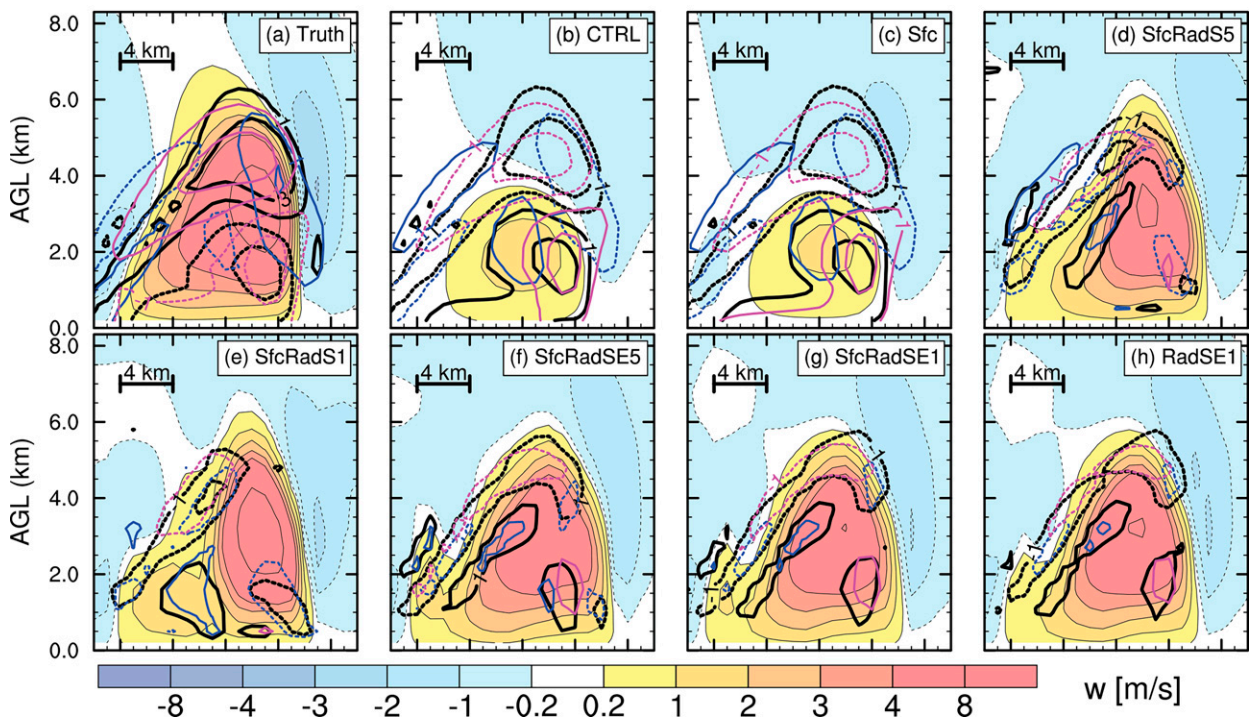
Surface-based Case @ t = 15 min

FIG. 7. (a) Height–*x* cross sections, along the maximum vertical velocity center in the truth simulation shown in Fig. 6 by magenta times signs, of horizontal wind divergence ($\partial u/\partial x + \partial v/\partial y$; black contours = $-3, -1, 1$, and 3×10^{-3} s^{-1}, with dashed contours being used for negative values), its *x* component ($\partial u/\partial x$; blue contours = $-3, -1, 1$, and 3×10^{-3} s^{-1}, with dashed contours being used for negative values) and *y* component ($\partial v/\partial y$; magenta contours = $-3, -1, 1$, and 3×10^{-3} s^{-1}, with dashed contours being used for negative values) and vertical velocity (shaded; m s^{-1}) in the truth simulation at $t = 15$ min. Also shown are height–*x* cross sections of vertical velocity (shaded; m s^{-1}) and the differences of horizontal wind divergence (black contours = $-3, -1, 1$, and 3×10^{-3} s^{-1}, with dashed contours being used for negative values), its *x* components (blue contours = $-3, -1, 1$, and 3×10^{-3} s^{-1}, with dashed contours being used for negative values), and its *y* components (magenta contours = $-3, -1, 1$, and 3×10^{-3} s^{-1}, with dashed contours being used for negative values) from the truth simulation for ensemble means of (b) CTRL, (c) Sfc, (d) SfcRadS5, (e) SfcRadS1, (f) SfcRadSE5, (g) SfcRadSE1, and (h) RadSE1. Minor *x* tick marks are included every 1 km, and major *x* tick marks are included every 4 km.

wind (Figs. 6a7,a8,b7,b8) and divergence fields (Figs. 7g,h) between SfcRadSE1 and RadSE1 reveal the little impact of assimilating surface mesonet observations on the CI forecasts again.

b. Elevated CI case

1) FORECAST SKILL EVALUATION

Figure 8 shows the extended FSS of ensemble forecasts from $t = 15$ to 30 min in 1-min intervals for the elevated CI case. CTRL and Sfc completely miss the CI by $t = 30$ min throughout the entire forecast period with FSS = 0. All experiments assimilating clear-air radial velocity observations significantly improve CI forecasts. SfcRadS1 performs the best overall with its FSSs not less than 0.9 from $t = 20$ to 30 min. SfcRadS5 (FSS = ~0.66), SfcRadS1 (FSS = ~0.9) and SfcRadSE5 (FSS = ~0.33) all begin to capture the CI at the same first CI time as the truth simulation ($t = 20$ min) with SfcRadS1 has the highest skill (FSS = ~0.9) followed by SfcRadS5 (FSS = ~0.66). From $t = 20$ to 22 min, SfcRadS1

has higher FSS than SfcRadS5, while SfcRadS1 has comparable or slightly worse skills after $t = 22$ min. Surprisingly, SfcRadSE5 has significantly higher CI forecast skill than SfcRadSE1 by $t = 27$ min while SfcRadSE1 has slightly higher skill after that. Generally, SfcRadS5 has higher FSSs than SfcRadSE5 and SfcRadS1 has higher FSSs than SfcRadSE1 from $t = 20$ to 26 min except that SfcRadSE5 has higher FSS than SfcRadS5 at $t = 21$ min. Higher FSSs can be attributed to more accurate prediction of CI timing, location, or both. As in the surface-based CI case, differences in probabilistic forecasts and analysis dynamic fields will be examined in later sections to understand the different skill improvements among the experiments. SfcRadSE1 has slightly higher FSSs than RadSE1 from $t = 21$ to 30 min, indicating that assimilating surface mesonet observations has a slightly positive impact on this elevated CI forecast. However, the impact is much smaller relative to assimilating clear-air radar data. The similarity and differences of the statistical results between the surface-based and elevated CI cases are discussed in later sections.
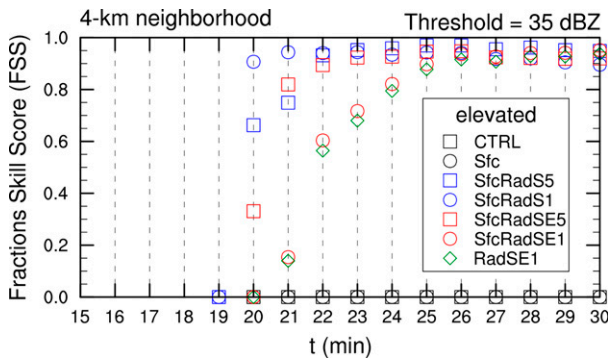
FIG. 8. As in Fig. 3, but for the elevated CI case.

2) PROBABILISTIC FORECASTS OF CONVECTION INITIATION

The probability of CREF $\geq$ 35 dBZ in the ensemble forecasts of the elevated case at t = 20, 21, 22, 25, and 30 min is shown in Fig. 9. No members of ensemble forecasts in CTRL and Sfc capture the CI process with the probability of 0 by t = 30 min (Figs. 9a1–e2) consistent with their FSS = 0 (Fig. 8). Similar to the surface-based CI case, all other experiments assimilating clear-air radial velocity data predict the CI process successfully at certain forecast lead time (Figs. 9a3–e7). These results indicate assimilating clear-air radial velocity data can basically capture the meso-γ-scale convergence in both cases. In contrast with the surface-based case, there are more CI grid points outside of the true swaths of CREF $\geq$ 35 dBZ (Figs. 9a3–e5), indicating more location bias of the prediction due to longer development of the CI process in the elevated case (Fig. 1). Consistent with FSSs shown in Fig. 8, some members in SfcRadS5 and SfcRadS1 predict CI at t = 20 min. This is the same as the first CI timing in the truth (Figs. 9a3,a4), which is similar to the surface-based case except with larger CI location biases. Some members in SfcRadSE5 capture early CI process at t = 20 min in the elevated case despite a location bias (Fig. 9a5). The improved performance of SfcRadSE5 for the elevated CI case may benefit from more vertical updraft component captured by radar radial winds with larger elevation angles. Similar to the surface-based case, CI in SfcRadSE1 in the elevated case is 1 min later than the truth (Fig. 9b6). At t = 30 min, the probability over 95% in all experiments assimilating clear-air radial velocity data match the swath of CREF $\geq$ 35 dBZ in the truth simulation very well (Figs. 9e3–e7). However, SfcRadS5, SfcRadS1, and SfcRadSE5 show more apparent eastward location bias (Figs. 9e3,e4), implying larger u-wind biases in these experiments. The length of this swath's west–east axis is ~17 km at t = 30 min, belonging to meso-γ scale. Therefore, similar to the surface-based CI case, assimilating clear-air radial velocity observations can also significantly improve the meso-γ-scale CI forecast in this elevated case.

From the probability difference between SfcRadS1 and SfcRadS5 (Figs. 10a1–d1), SfcRadS1 has larger probability in most areas within the swath of CREF $\geq$ 35 dBZ in the truth simulation by t = 22 min, indicating that assimilating higher

frequency clear-air radial velocity observations can improve the CI forecast during early stages. The positive and negative differences located to the east and west sides of the probability swath, respectively, from t = 25 to 30 min are due to more eastward location bias in SfcRadS1 than in SfcRadS5 (Figs. 10c1–d1). These results are similar to those in the surface-based case (Figs. 5a1–d1). From the difference between SfcRadSE1 and SfcRadSE5, most areas within the true swath of CREF $\geq$ 35 dBZ contain negative values of probability difference by t = 22 min (Figs. 10a2–b2) as a result of 1-min CI timing bias in SfcRadSE1 relative to SfcRadSE5. After t = 25 min (Figs. 10c2–d2), the negative probability differences are mainly outside and to the east of the swath, indicating that assimilating clear-air radial velocity observations from both radars at higher frequency produces more accurate location prediction than at lower frequency. Differences between SfcRadSE1 and SfcRadS1 (Figs. 10a3–d3) resembles those between SfcRadSE1 and SfcRadS5 (Figs. 10a2–d2), implying location biases can be reduced mainly by assimilating radial velocity data from the eastern radar at higher frequency. Assimilating extra surface mesonet observations can only slightly improve the CI forecast with small positive probability differences (Figs. 10a3–d3).

3) WIND AND CONVERGENCE FIELDS

Three-dimensional winds and horizontal convergences are examined to explain the differences in FSSs and probabilistic forecasts among different experiments.

At the end of the final DA cycle (t = 15 min) in the elevated case, maximum vertical velocities are over 1 and 4 m s^{-1} at 1.5 and 3.5 km AGL, respectively, and reach 4.7 m s^{-1} within the model volume in the truth simulation (Figs. 11a1,b1), which are weaker than those in the surface-based case (Figs. 6a1,b1). More latent heat release below 1.5 km AGL results in stronger buoyancy in the lower levels in the surface-based case. The truth simulation displays obvious horizontally convergent winds at 1.5 km AGL (Fig. 11a1) with the maximum convergence stronger than 1×10^{-3} s^{-1} near the strong updraft center (Fig. 12a). This convergence mainly results from the y component of convergence (Fig. 12a). At 3.5 km AGL in the truth simulation, there exist horizontally divergent winds near the strong vertical velocity center with the maximum divergence over 1×10^{-3} s^{-1} (Figs. 11b1 and 12a), which is weaker than that in the surface-based case (Figs. 6b1 and 7a). The weaker convergence in the lower levels, weaker divergence in the upper levels, and weaker vertical updrafts are all due to the weaker buoyancy, resulting in slower development of convection in the elevated case than the surface-based case (Fig. 1).

The deviations of CTRL and Sfc from the truth are very similar in both wind and divergence fields. The maximum absolute errors of vertical velocity are over 1 and 4 m s^{-1} at 1.5 and 3.5 km AGL, respectively. The maximum absolute errors of divergence are over 1×10^{-3} s^{-1} at both 1.5 and 3.5 km AGL. These results again confirm that assimilating only surface mesonet observations has little impact on the wind field and divergence (Figs. 11a2,a3,b2,b3 and 12b,c). After assimilating clear-air radial velocity from the
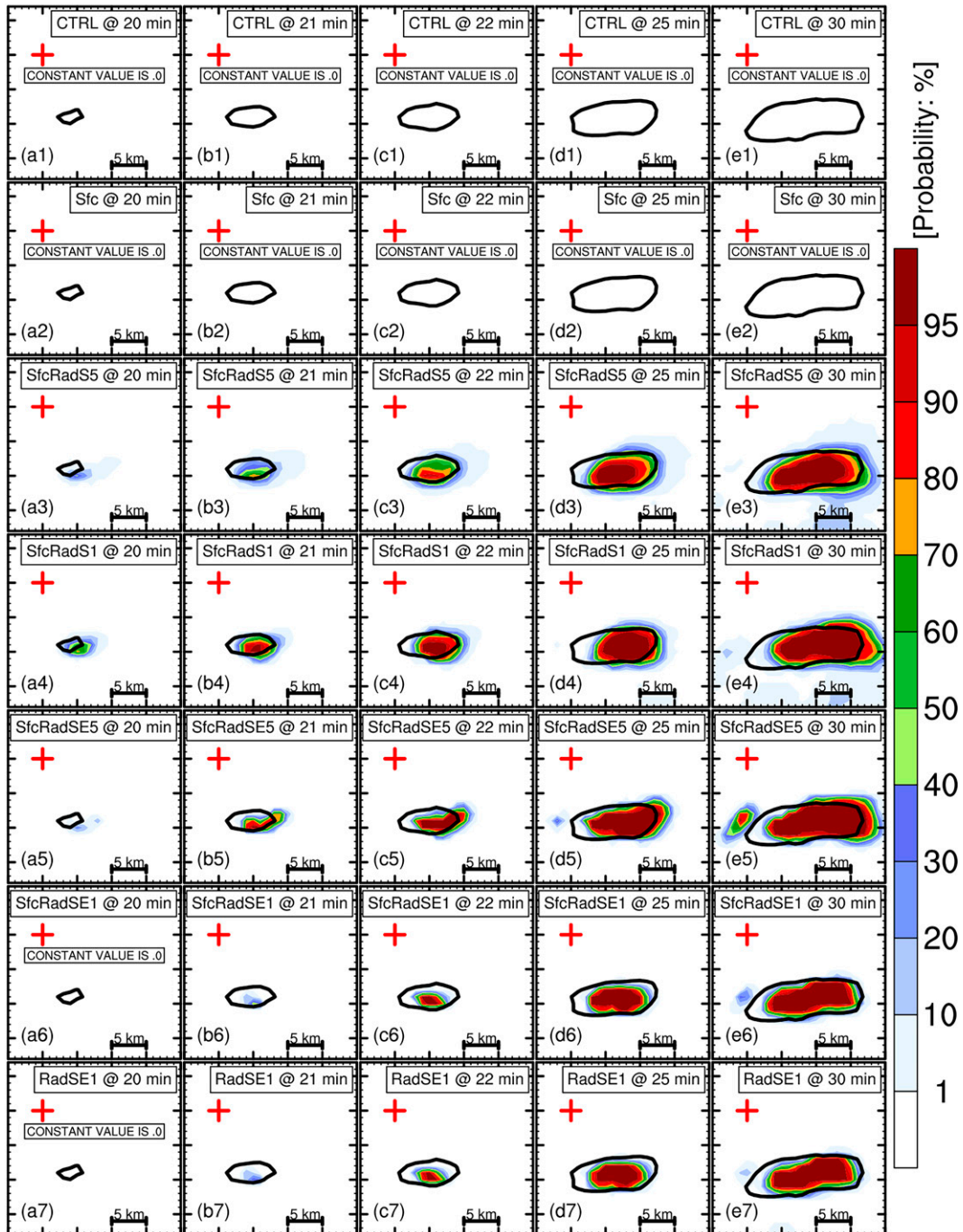
Elevated Case

FIG. 9. As in Fig. 4, but for the elevated CI case at t = 20, 21, 22, 25, and 30 min. Minor tick marks are included every 1 km, and major tick marks are included every 5 km.

southern radar every 5 min in addition to the surface observations (SfcRadS5), the wind errors are reduced significantly near the strong updraft center with maximum absolute errors of vertical velocity less than 1 and 2 m s^{-1} at 1.5 and 3.5 km AGL, respectively (Figs. 11a4,b4). The areas with absolute errors of divergence fields in SfcRadS5

over 1×10^{-3} s^{-1} are reduced dramatically (Fig. 12d) relative to those in Sfc (Fig. 12c).

It also can be found that there are larger errors of wind and divergence fields on the east of updraft center in SfcRadS5 with maximum absolute errors of vertical velocity and divergences larger than 1 m s^{-1} and 1×10^{-3} s^{-1}, respectively, at
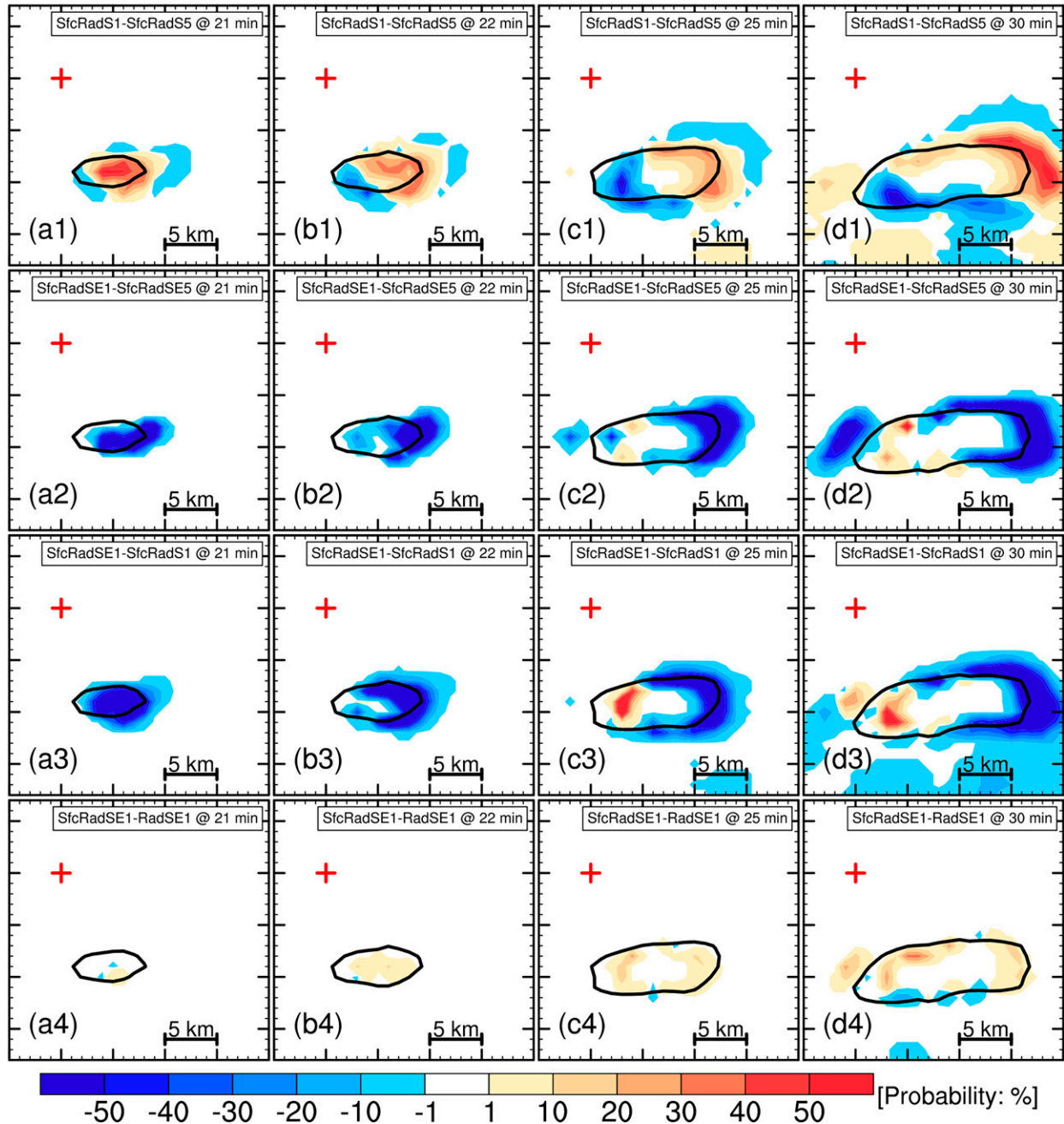
Elevated Case

FIG. 10. As in Fig. 5, but for the elevated CI case at t = 21, 22, 25, and 30 min. Minor tick marks are included every 1 km, and major tick marks are included every 5 km.

both 1.5 and 3.5 km AGL (Figs. 11a4,b4 and 12d). The larger errors in u winds (Fig. 11a4) result in eastward CI location biases in SfcRadS5 shown in Figs. 9a3–e3. These errors increase in SfcRadS1 with larger areas with absolute u-wind errors more than 1 m s^{-1}, maximum absolute errors of vertical velocity larger than 2 m s^{-1} at 1.5 km AGL (Fig. 11a5), and larger areas with absolute divergence anomaly over 1×10^{-3} s^{-1} below 2 km AGL (Fig. 12e), which results in larger

location biases of convection in SfcRadS1 shown in Figs. 9a4–e4 and 10a1–d1. Similar to the surface-based case, the ensemble cannot capture the covariance between radial velocity of the southern radar and u winds near the strong updraft center well (not shown), due to the cross-beam nature of these winds. Therefore, larger u-wind biases exist in SfcRadS5 (Figs. 11a4,b4), and the biases increase with the greater assimilation frequency in SfcRadS1 (Figs. 11a5,b5).
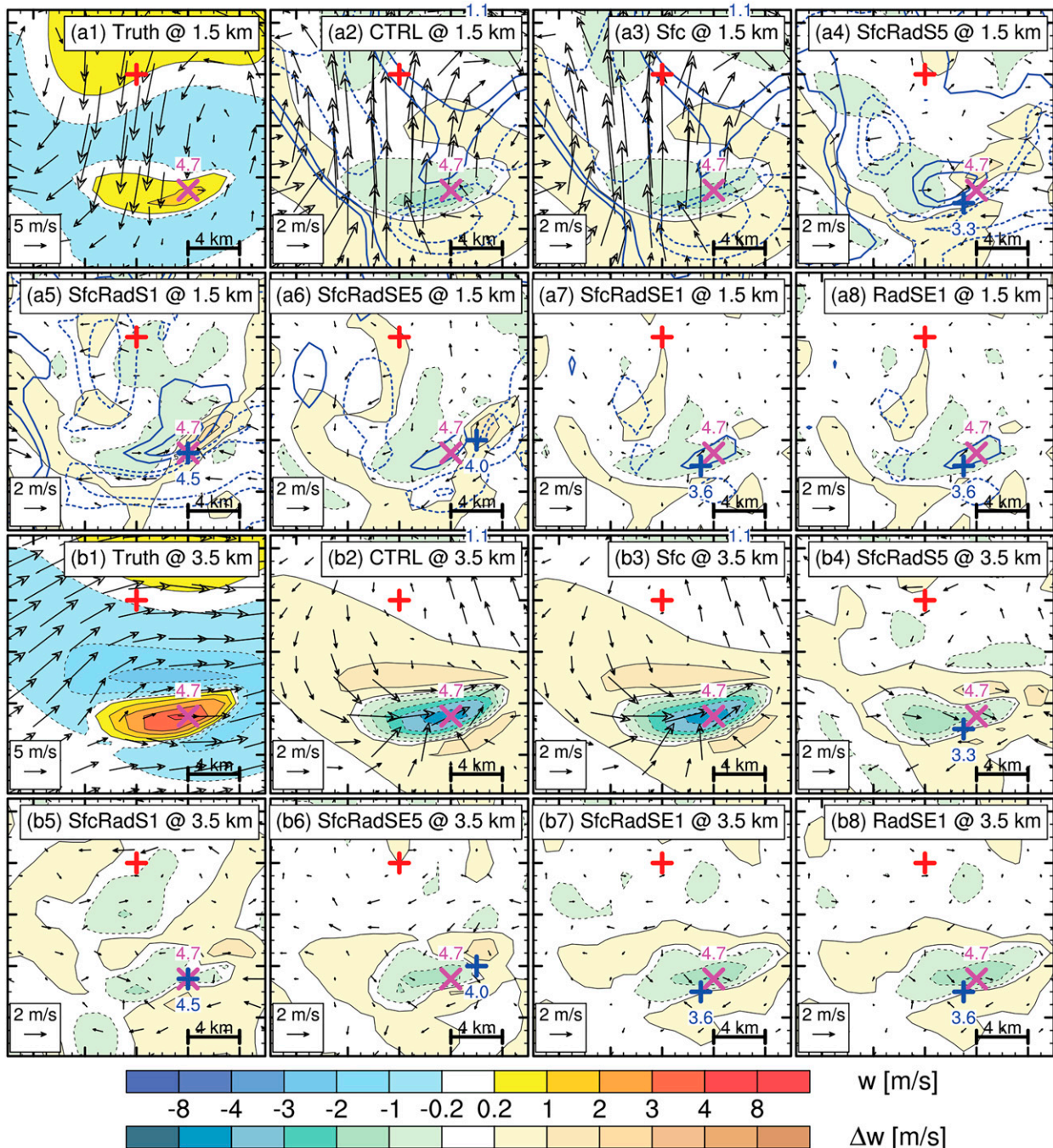
Elevated Case @ t = 15 min

FIG. 11. As in Fig. 6, but for the elevated CI case at (a1)–(a8) 1.5 and (b1)–(b8) 3.5 km AGL.

However, these u-wind errors lead to stronger convergence in the lower levels (Fig. 12e) and maximum vertical updrafts closer to the truth (Fig. 12e), making CI timing closer to the truth simulation. The closer CI timing to the truth results in higher FSSs in SfcRadS1 than SfcRadS5 at the beginning of CI process by $t = 23$ min (Fig. 8). Meanwhile, the u-wind errors also result in larger location biases at the later stage,

leading to slightly lower FSSs in SfcRadS1 than SfcRadS5 after $t = 23$ min (Fig. 8). Therefore, similar to the surface-based case, the higher FSSs in SfcRadS1 are not due to the more accurate analysis of meso-γ-scale horizontal convergence. Although the DA also updates the vertical velocity fields, the model's response to the DA dominates the vertical velocity evolution (not shown).
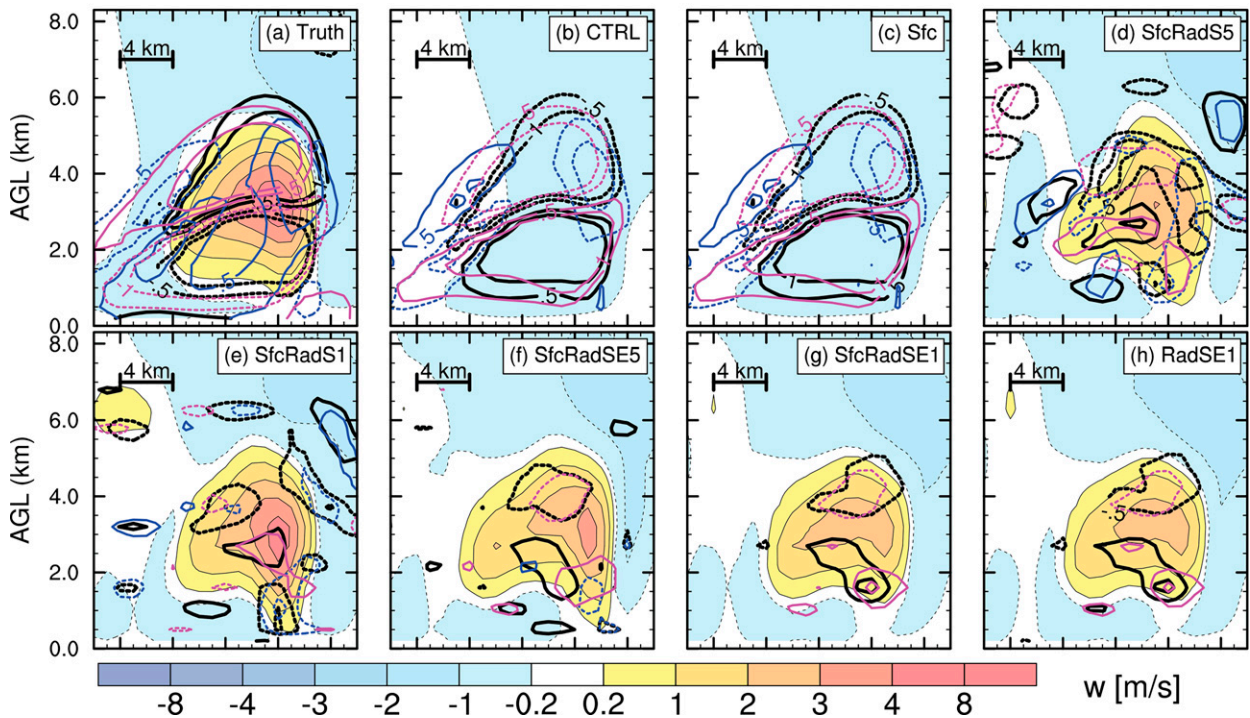
FIG. 12. As in Fig. 7, but for the elevated CI case for (a) truth, (b) CTRL, (c) Sfc, (d) SfcRadS5, (e) SfcRadS1, (f) SfcRadSE5, (g) SfcRadSE1, and (h) RadSE1. Black, blue, and magenta contours = -1, -0.5, 0.5, and 1×10^{-3} s^{-1}, with dashed contours being used for negative values.

After assimilating additional clear-air radial velocity from the eastern radar (SfcRadSE5 and SfcRadSE1), errors in horizontal wind and divergence fields are reduced, particularly near the strong updraft center, relative to SfcRadS5 and SfcRadS1 (Figs. 11a4–a7,b4–b7 and 12d–g). The errors on the east side of the strong updraft center are also reduced, indicating that u winds can be corrected by assimilating clear-air radial velocity from the eastern radar. Meanwhile, assimilating high-time-frequency clear-air radial velocity observations in SfcRadSE1 has better u-wind analysis than SfcRadSE5. Therefore, smaller location biases are in SfcRadSE5 than SfcRadS5, SfcRadSE1 than SfcRadS1, and SfcRadSE1 than SfcRadSE5 (Fig. 10). Similarly, larger u-wind biases in SfcRadSE5 than SfcRadSE1 due to assimilating lower-time-frequency radial velocity from the eastern radar result in stronger x-component convergence in the lower levels and updrafts (Figs. 12f,g), and closer CI timing to the truth but larger location biases, which is consistent with higher FSSs by $t = 27$ min and slightly lower FSSs after $t = 27$ min in SfcRadSE5 than SfcRadSE1 (Fig. 8). However, assimilating clear-air radial velocity from the eastern radar increases the analysis errors in v winds in the lower levels in SfcRadSE5 and SfcRadSE1 due to the limited ability of the ensemble to capture the covariance between radial velocity of the eastern radar and v winds near strong updraft center (Figs. 12f,g). These errors are stronger in SfcRadSE1 than SfcRadSE5 leading to stronger divergence and weaker updraft

in SfcRadSE1 (Figs. 12f,g), so CI timing is earlier in SfcRadSE5. No obvious differences in wind (Figs. 11a7,a8,b7,b8) and divergence fields (Figs. 12g,h) between SfcRadSE1 and RadSE1 are found. Different from the surface-based CI case, assimilating surface observations in addition to radial velocity observations can slightly improve the CI forecast in the elevated case (Figs. 8 and 10a4–d4). Diagnostics suggest that the surface observation with mesonet resolution captures the relatively large-scale characteristics near the surface while the maximum meso-γ-scale convergence occurs at 1.5 km AGL.

4. Summary

In this study, observing system simulation experiments are conducted to study the potential benefits of assimilating PAR clear-air radial velocity observations to the forecast of CI along small-scale boundary layer convergence zones. To examine whether high spatiotemporal resolution PAR clear-air radial velocity observations can partly fill the gaps in the current operational observing systems, two typical types of CI, surface-based and elevated CI cases driven by meso-γ-scale boundary layer convergence, respectively, are tested. Synthetic surface mesonet observations at ~30-km and 5-min resolutions and PAR clear-air radial velocity observations at a 1-min resolution of both surface-based and elevated CI cases are created using the Weather Research and Forecasting Model. These observations are assimilated over a 10-min

period before the first CI occurrence using an ensemble Kalman filter method. The main results are summarized as follows:

1) Assimilating only surface mesonet observations fails to predict either surface-based or elevated meso-γ-scale CI processes. Although it is hard to determine systematic positive or negative impacts of assimilating surface mesonet observations on CI forecasts due to the limited number of cases in this study, it can be concluded that assimilating coarse-resolution surface mesonet observations has little impact on the wind and divergence fields of the analyses in both surface-based and elevated cases, and therefore has little impact on the subsequent CI forecasts.

2) All the experiments containing clear-air radial velocity observations can capture both surface-based and elevated CI processes successfully, although some experiments have biases of CI timing and location. Such an improvement benefits from the better analyses of meso-γ-scale boundary layer convergence in both surface-based and elevated CI cases resulting from assimilating PAR clear-air radial velocity observations.

3) The experiments assimilating clear-air radial velocity observations only from the southern radar have higher forecast scores than those assimilating observations from both the southern and eastern radars. The forecast scores associated with assimilating only the southern radar increase with greater assimilation frequency especially at the early stage of CI processes. Diagnostics suggest that the higher forecast scores are attributed to the larger u-wind biases leading to stronger low-level convergence and updrafts that are closer to the truth. Such u-wind biases are a result of the inability of the ensemble to properly represent the covariance between the radial velocity of the southern radar and u winds near the strong updraft center. These u-wind biases increase with assimilating radial velocity only from the southern radar more frequently, leading to faster moving and larger location errors of convection. Assimilating clear-air radial velocity observations from both the southern and eastern radars in particular with higher-time-frequency can improve the u-wind analysis and then improve the forecast of convection location. However, the analysis errors in v winds in the lower levels increase similarly when assimilating clear-air radial velocity from the eastern radar. These results suggest the need to optimize the radar network design and to further improve ensemble-based data assimilation for radar observations. Note that densely located PAR network costs are high. Further, some recent studies (e.g., Maejima and Miyoshi 2020; et al. 2021) indicated that when DA parameters were tuned well and a sufficiently large ensemble (e.g., 1000 members in Ruiz et al. 2021) was employed, assimilating dense observations at a higher frequency improved analysis accuracy by reducing nonlinearlity and non-Gaussianity. Meanwhile, if the ensemble size is large enough, the quality of covariance between the radial velocity observations and the winds would improve as well and wind analysis bias would be reduced. Therefore, the results of a single radar from this study still suggests the potential of PAR on observing the boundary layer convergence zones to help CI forecasts.

To our knowledge, this study is the first to investigate the benefits of assimilating PAR clear-air radial velocity observations to improve the forecast of CI along small-scale boundary layer convergence zones. The results highlight the potential for assimilating these observations to improve CI forecasts. Note that only idealized CI cases determined by the convergence of wind fields are considered with perfect model assumption in this study. Only horizontal winds are perturbed to create ensemble members initialized with a horizontally homogeneous base state, and temperature and humidity fields are assumed to be perfect at the initial time. We are aware that, the conclusions obtained in this study are based on these idealized-case OSSEs and the assumption of a perfect model. A realistic scenario including heterogeneous atmospheric environment, combination of different CI mechanisms, different radar networks, uncertainties on various scales, as well as the model error, may reduce the potential value of assimilating PAR clear-air radial velocity observations on CI forecasts. However, this study provides insights on the relative impact of PAR clear-air radial velocity and surface mesonet observations. It therefore reveals the potential benefit of PAR clear-air radial velocity observations on CI forecasts in NWP system filling the gaps in current operational observing systems where high-resolution upper-air observations especially in planetary boundary layer are lacking. In the future, real-case studies, such as real PAR data cases and/or OSSEs created from more realistic CI simulations (e.g., high-resolution dryline or frontal boundary simulation), should be conducted to verify the conclusions attained in this study.

Data availability statement. The model output data generated in this study are too large to be publicly archived with available resources. Please contact the corresponding author for more information.

REFERENCES

Abulikemu, A., Y. Wang, R. Gao, Y. Wang, and X. Xu, 2019: A numerical study of convection initiation associated with a gust front in Bohai Bay region, North China. *J. Geophys. Res. Atmos.*, **124**, 13 843–13 860, https://doi.org/10.1029/2019JD030883.

Anderson, J. L., 2001: An ensemble adjustment Kalman filter for data assimilation. *Mon. Wea. Rev.*, **129**, 2884–2903, https://doi.org/10.1175/1520-0493(2001)129<2884:AEAKFF>2.0.CO;2.

——, 2009: Spatially and temporally varying adaptive covariance inflation for ensemble filters. *Tellus*, **61A**, 72–83, https://doi.org/10.1111/j.1600-0870.2008.00361.x.

——, T. Hoar, K. Raeder, H. Liu, N. Collins, R. Torn, and A. Avellano, 2009: The Data Assimilation Research Testbed: A community facility. *Bull. Amer. Meteor. Soc.*, **90**, 1283–1296, https://doi.org/10.1175/2009BAMS2618.1.

Bachmann, K., C. Keil, and M. Weissmann, 2019: Impact of radar data assimilation and orography on predictability of deep convection. *Quart. J. Roy. Meteor. Soc.*, **145**, 117–130, https://doi.org/10.1002/qj.3412.

Balsamo, G., and Coauthors, 2018: Satellite and in situ observations for advancing global Earth surface modelling: A review. *Remote Sens.*, **10**, 2038, https://doi.org/10.3390/rs10122038.

Browning, K. A., and Coauthors, 2007: The Convective Storm Initiation Project. *Bull. Amer. Meteor. Soc.*, **88**, 1939–1956, https://doi.org/10.1175/BAMS-88-12-1939.

Coniglio, M. C., G. S. Romine, D. D. Turner, and R. D. Torn, 2019: Impacts of targeted AERI and Doppler lidar wind retrievals on short-term forecasts of the initiation and early evolution of thunderstorms. *Mon. Wea. Rev.*, **147**, 1149–1170, https://doi.org/10.1175/MWR-D-18-0351.1.

Degelia, S., X. Wang, D. Stensrud, and A. Johnson, 2018: Understanding the impact of radar and in-situ observations on the prediction of a nocturnal convection initiation event on 25 June 2013 using an ensemble-based multiscale data assimilation system. *Mon. Wea. Rev.*, **146**, 1837–1859, https://doi.org/10.1175/MWR-D-17-0128.1.

——, ——, and ——, 2019: An evaluation of the impact of assimilating AERI retrievals, kinematic profilers, rawinsondes, and surface observations on a forecast of a nocturnal convection initiation event during the PECAN field campaign. *Mon. Wea. Rev.*, **147**, 2739–2764, https://doi.org/10.1175/MWR-D-18-0423.1.

——, ——, ——, and D. D. Turner, 2020: Systematic evaluation of the impact of assimilating a network of ground-based remote sensing profilers for forecasts of nocturnal convection initiation during PECAN. *Mon. Wea. Rev.*, **148**, 4703–4728, https://doi.org/10.1175/MWR-D-20-0118.1.

Dowell, D. C., F. Zhang, L. J. Wicker, C. Snyder, and N. A. Crook, 2004: Wind and temperature retrievals in the 17 May 1981 Arcadia, Oklahoma, supercell: Ensemble Kalman filter experiments. *Mon. Wea. Rev.*, **132**, 1982–2005, https://doi.org/10.1175/1520-0493(2004)132<1982:WATRIT>2.0.CO;2.

——, L. J. Wicker, and C. Snyder, 2011: Ensemble Kalman filter assimilation of radar observations of the 8 May 2003 Oklahoma City supercell: Influences of reflectivity observations on storm-scale analyses. *Mon. Wea. Rev.*, **139**, 272–294, https://doi.org/10.1175/2010MWR3438.1.

Duc, L., K. Saito, and H. Seko, 2013: Spatial-temporal fractions verification for high-resolution ensemble forecasts. *Tellus*, **65A**, 18171, https://doi.org/10.3402/tellusa.v65i0.18171.

Fovell, R. G., 2005: Convective initiation ahead of the sea-breeze front. *Mon. Wea. Rev.*, **133**, 264–278, https://doi.org/10.1175/MWR-2852.1.

Gaspari, G., and S. E. Cohn, 1999: Construction of correlation functions in two and three dimensions. *Quart. J. Roy. Meteor. Soc.*, **125**, 723–757, https://doi.org/10.1002/qj.49712555417.

Gasperoni, N. A., X. Wang, K. A. Brewster, and F. H. Carr, 2018: Assessing impacts of the high-frequency assimilation of surface observations for the forecast of convection initiation on 3 April 2014 within the Dallas–Fort Worth test bed. *Mon. Wea. Rev.*, **146**, 3845–3872, https://doi.org/10.1175/MWR-D-18-0177.1.

Geerts, B., and Coauthors, 2017: The 2015 Plains Elevated Convection at Night Field Project. *Bull. Amer. Meteor. Soc.*, **98**, 767–786, https://doi.org/10.1175/BAMS-D-15-00257.1.

Hill, A. J., C. C. Weiss, and B. C. Ancell, 2016: Ensemble sensitivity analysis for mesoscale forecasts of dryline convection initiation. *Mon. Wea. Rev.*, **144**, 4161–4182, https://doi.org/10.1175/MWR-D-15-0338.1.

Huang, Y., Y. Liu, Y. Liu, H. Li, and J. C. Knievel, 2019: Mechanisms for a record-breaking rainfall in the coastal metropolitan city of Guangzhou, China: Observation analysis and nested very large eddy simulation with the WRF model. *J. Geophys. Res. Atmos.*, **124**, 1370–1391, https://doi.org/10.1029/2018JD029668.

——, X. Wang, C. Kerr, A. Mahre, T. Yu, and D. Bodine, 2020: Impact of assimilating future clear-air radial velocity observations from phased array radar on a supercell thunderstorm forecast: An observing system simulation experiment study. *Mon. Wea. Rev.*, **148**, 3825–3845, https://doi.org/10.1175/MWR-D-19-0391.1.

Jiménez, P. A., J. Dudhia, J. F. Gonzalez–Rouco, J. Navarro, J. P. Montavez, and E. Garcia-Bustamante, 2012: A revised scheme for the WRF surface layer formulation. *Mon. Wea. Rev.*, **140**, 898–918, https://doi.org/10.1175/MWR-D-11-00056.1.

Johnson, A., X. Wang, J. R. Carley, L. J. Wicker, and C. Karstens, 2015: A comparison of multiscale GSI-based EnKF and 3DVar data assimilation using radar and conventional observations for midlatitude convective-scale precipitation forecasts. *Mon. Wea. Rev.*, **143**, 3087–3108, https://doi.org/10.1175/MWR-D-14-00345.1.

Kang, S.-L., and G. H. Bryan, 2011: A large-eddy simulation study of moist convection initiation over heterogeneous surface fluxes. *Mon. Wea. Rev.*, **139**, 2901–2917, https://doi.org/10.1175/MWR-D-10-05037.1.

Keclik, A. M., C. Evans, P. J. Roebber, and G. S. Romine, 2017: The influence of assimilated upstream, preconvective dropsonde observations on ensemble forecasts of convection initiation during the mesoscale predictability experiment. *Mon. Wea. Rev.*, **145**, 4747–4770, https://doi.org/10.1175/MWR-D-17-0159.1.

Kirshbaum, D. J., 2011: Cloud-resolving simulations of deep convection over a heated mountain. *J. Atmos. Sci.*, **68**, 361–378, https://doi.org/10.1175/2010JAS3642.1.

Koch, S. E., and W. L. Clark, 1999: A nonclassical cold front observed during COPS-91: Frontal structure and the process of severe storm initiation. *J. Atmos. Sci.*, **56**, 2862–2890, https://doi.org/10.1175/1520-0469(1999)056<2862:ANCFOD>2.0.CO;2.

——, M. Fengler, P. B. Chilson, K. L. Elmore, B. Argrow, D. L. Andra, and T. Lindley, 2018: On the use of unmanned aircraft for sampling mesoscale phenomena in the preconvective boundary layer. *J. Atmos. Oceanic Technol.*, **35**, 2265–2288, https://doi.org/10.1175/JTECH-D-18-0101.1.

Kollias, P., D. J. McLaughlin, S. Frasier, M. Oue, E. Luke, and A. Sneddon, 2018: Advances and applications in low-power phased array X-band weather radars. *2018 IEEE Radar Conf. (RadarConf18)*, Oklahoma City, OK, Institute of Electrical and Electronics Engineers, 1359–1364, https://doi.org/10.1109/RADAR.2018.8378762.

Kong, R., M. Xue, and C. Liu, 2018: Development of a hybrid En3DVar data assimilation system and comparisons with 3DVar and EnKF for radar data assimilation with observing

system simulation experiments. *Mon. Wea. Rev.*, **146**, 175–198, https://doi.org/10.1175/MWR-D-17-0164.1.

Leuenberger, D., A. Haefele, N. Omanovic, M. Fengler, G. Martucci, B. Calpini, O. Fuhrer, and A. Rossa, 2020: Improving high-impact numerical weather prediction with lidar and drone observations. *Bull. Amer. Meteor. Soc.*, **101**, E1036–E1051, https://doi.org/10.1175/BAMS-D-19-0119.1.

Lippi, D. E., J. R. Carley, and D. T. Kleist, 2019: Improvements to the assimilation of Doppler radial winds for convection-permitting forecasts of a heavy rain event. *Mon. Wea. Rev.*, **147**, 3609–3632, https://doi.org/10.1175/MWR-D-18-0411.1.

Liu, C., M. Xue, and R. Kong, 2019: Direct assimilation of radar reflectivity data using 3DVAR: Treatment of hydrometeor background errors and OSSE tests. *Mon. Wea. Rev.*, **147**, 17–29, https://doi.org/10.1175/MWR-D-18-0033.1.

Lock, N. A., and A. L. Houston, 2014: Empirical examination of the factors regulating thunderstorm initiation. *Mon. Wea. Rev.*, **142**, 240–258, https://doi.org/10.1175/MWR-D-13-00082.1.

Madaus, L. E., and G. J. Hakim, 2017: Constraining ensemble forecasts of discrete convective initiation with surface observations. *Mon. Wea. Rev.*, **145**, 2597–2610, https://doi.org/10.1175/MWR-D-16-0395.1.

Maejima, Y., and T. Miyoshi, 2020: Impact of the window length of four-dimensional local ensemble transform Kalman filter: A case of convective rain event. *SOLA*, **16**, 37–42, https://doi.org/10.2151/sola.2020-007.

Mahre, A., T.-Y. Yu, and D. J. Bodine, 2020: A comparison of scan speedup strategies and their effect on rapid-scan weather radar data quality. *J. Atmos. Oceanic Technol.*, **37**, 1955–1972, https://doi.org/10.1175/JTECH-D-19-0216.1.

Markowski, P., and Y. Richardson, 2010: *Mesoscale Meteorology in Midlatitudes*. Wiley-Blackwell, 407 pp.

——, C. Hannon, and E. Rasmussen, 2006: Observations of convection initiation "failure" from the 12 June 2002 IHOP deployment. *Mon. Wea. Rev.*, **134**, 375–405, https://doi.org/10.1175/MWR3059.1.

McPherson, R. A., and Coauthors, 2007: Statewide monitoring of the mesoscale environment: A technical update on the Oklahoma Mesonet. *J. Atmos. Oceanic Technol.*, **24**, 301–321, https://doi.org/10.1175/JTECH1976.1.

Morrison, H., J. A. Milbrandt, G. H. Bryan, K. Ikeda, S. A. Tessendorf, and G. Thompson, 2015: Parameterization of cloud microphysics based on the prediction of bulk ice particle properties. Part II: Case study comparisons with observations and other schemes. *J. Atmos. Sci.*, **72**, 312–339, https://doi.org/10.1175/JAS-D-14-0066.1.

NRC, 2009: *Observing Weather and Climate from the Ground Up—A Nationwide Network of Networks*. National Academies Press, 250 pp., https://doi.org/10.17226/12540.

Pan, S., J. Gao, D. J. Stensrud, X. Wang, and T. A. Jones, 2018: Assimilation of radar radial velocity and reflectivity, satellite cloud water path, and total precipitable water for convective-scale NWP in OSSEs. *J. Atmos. Oceanic Technol.*, **35**, 67–89, https://doi.org/10.1175/JTECH-D-17-0081.1.

Parsons, D. B., K. R. Haghi, K. T. Halbert, B. Elmer, and J. Wang, 2019: The potential role of atmospheric bores and gravity waves in the initiation and maintenance of nocturnal convection over the Southern Great Plains. *J. Atmos. Sci.*, **76**, 43–68, https://doi.org/10.1175/JAS-D-17-0172.1.

Reif, D. W., and H. B. Bluestein, 2018: Initiation mechanisms of nocturnal convection without nearby surface boundaries over the central and southern Great Plains during the warm season. *Mon. Wea. Rev.*, **146**, 3053–3078, https://doi.org/10.1175/MWR-D-18-0040.1.

Roberts, N. M., and H. W. Lean, 2008: Scale-selective verification of rainfall accumulations from high-resolution forecasts of convective events. *Mon. Wea. Rev.*, **136**, 78–97, https://doi.org/10.1175/2007MWR2123.1.

Ruiz, J., G.-Y. Lien, K. Kondo, S. Otsuka, and T. Miyoshi, 2021: Reduced non-Gaussianity by 30 s rapid update in convective-scale numerical weather prediction. *Nonlinear Processes Geophys.*, **28**, 615–626, https://doi.org/10.5194/npg-28-615-2021.

Schröttle, J., M. Weissmann, L. Scheck, and A. Hutt, 2020: Assimilating visible and infrared radiances in idealized simulations of deep convection. *Mon. Wea. Rev.*, **148**, 4357–4375, https://doi.org/10.1175/MWR-D-20-0002.1.

Skamarock, W. C., and Coauthors, 2008: A description of the Advanced Research WRF version 3. NCAR Tech. Note NCAR/TN-475+STR, 113 pp., https://doi.org/10.5065/D68S4MVH.

Sobash, R. A., and D. J. Stensrud, 2015: Assimilating surface mesonet observations with the EnKF to improve ensemble forecasts of convection initiation on 29 May 2012. *Mon. Wea. Rev.*, **143**, 3700–3725, https://doi.org/10.1175/MWR-D-14-00126.1.

Sun, J., and Coauthors, 2014: Use of NWP for nowcasting convective precipitation: Recent progress and challenges. *Bull. Amer. Meteor. Soc.*, **95**, 409–426, https://doi.org/10.1175/BAMS-D-11-00263.1.

Taylor, J., and Coauthors, 2021: Oversampling reflectivity observations from a geostationary precipitation radar satellite: Impact on typhoon forecasts within a perfect model OSSE framework. *J. Adv. Model. Earth Syst.*, **13**, e2020MS002332, https://doi.org/10.1029/2020MS002332.

Thompson, G., P. R. Field, R. M. Rasmussen, and W. D. Hall, 2008: Explicit forecasts of winter precipitation using an improved bulk microphysics scheme. Part II: Implementation of a new snow parameterization. *Mon. Wea. Rev.*, **136**, 5095–5115, https://doi.org/10.1175/2008MWR2387.1.

Trier, S. B., G. S. Romine, D. A. Ahijevych, R. J. Trapp, R. S. Schumacher, M. C. Coniglio, and D. J. Stensrud, 2015: Mesoscale thermodynamic influences on convection initiation near a surface dryline in a convection-permitting ensemble. *Mon. Wea. Rev.*, **143**, 3726–3753, https://doi.org/10.1175/MWR-D-15-0133.1.

Wang, Q.-W., and M. Xue, 2018: A high-resolution modeling study of the 19 June 2002 convective initiation case during IHOP_2002: Localized forcing by horizontal convective rolls. *Adv. Atmos. Sci.*, **35**, 1243–1253, https://doi.org/10.1007/s00376-018-7218-3.

Wang, Y., and X. Wang, 2017: Direct assimilation of radar reflectivity without tangent linear and adjoint of the nonlinear observation operator in the GSI-based EnVar system: Methodology and experiment with the 8 May 2003 Oklahoma City tornadic supercell. *Mon. Wea. Rev.*, **145**, 1447–1471, https://doi.org/10.1175/MWR-D-16-0231.1.

Weckwerth, T. M., 2000: The effect of small-scale moisture variability on thunderstorm initiation. *Mon. Wea. Rev.*, **128**, 4017–4030, https://doi.org/10.1175/1520-0493(2000)129<4017:TEOSSM>2.0.CO;2.

——, and D. B. Parsons, 2006: A review of convection initiation and motivation for IHOP_2002. *Mon. Wea. Rev.*, **134**, 5–22, https://doi.org/10.1175/MWR3067.1.

——, and Coauthors, 2004: An overview of the international H$_2$O Project (IHOP_2002) and some preliminary highlights. *Bull. Amer. Meteor. Soc.*, **85**, 253–278, https://doi.org/10.1175/BAMS-85-2-253.

——, J. Hanesiak, J. W. Wilson, S. B. Trier, S. K. Degelia, W. A. Gallus, R. D. Roberts, and X. Wang, 2019: Nocturnal convection initiation during PECAN 2015. *Bull. Amer. Meteor. Soc.*, **100**, 2223–2239, https://doi.org/10.1175/BAMS-D-18-0299.1.

Wilhelmson, R. B., and C. S. Chen, 1982: A simulation of the development of successive cells along a cold outflow boundary. *J. Atmos. Sci.*, **39**, 1466–1483, https://doi.org/10.1175/1520-0469(1982)039<1466:ASOTDO>2.0.CO;2.

Wilson, J. W., and R. D. Roberts, 2006: Summary of convective storm initiation and evolution during IHOP: Observational and modeling perspective. *Mon. Wea. Rev.*, **134**, 23–47, https://doi.org/10.1175/MWR3069.1.

——, T. M. Weckwerth, J. Vivekanandan, R. M. Wakimoto, and R. W. Russell, 1994: Boundary layer clear-air radar echoes: Origin of echoes and accuracy of derived winds. *J. Atmos. Oceanic Technol.*, **11**, 1184–1206, https://doi.org/10.1175/1520-0426(1994)011<1184:BLCARE>2.0.CO;2.

Xu, Q., H. Lu, S. Gao, M. Xue, and M. Tong, 2008: Time-expanded sampling for ensemble Kalman filter: Assimilation experiments with simulated radar observations. *Mon. Wea. Rev.*, **136**, 2651–2667, https://doi.org/10.1175/2007MWR2185.1.

Yu, T.-Y., M. B. Orescanin, C. D. Curtis, D. S. Zrnić, and D. E. Forsyth, 2007: Beam multiplexing using the phased-array weather radar. *J. Atmos. Oceanic Technol.*, **24**, 616–626, https://doi.org/10.1175/JTECH2052.1.

Yussouf, N., E. R. Mansell, L. J. Wicker, D. M. Wheatley, and D. J. Stensrud, 2013: The ensemble Kalman filter analyses and forecasts of the 8 May 2003 Oklahoma City tornadic supercell storm using single- and double-moment microphysics schemes. *Mon. Wea. Rev.*, **141**, 3388–3412, https://doi.org/10.1175/MWR-D-12-00237.1.

Zhao, J., J. Gao, T. A. Jones, and J. Hu, 2021: Impact of assimilating high-resolution atmospheric motion vectors on convective scale short-term forecasts: 1. Observing System Simulation Experiment (OSSE). *J. Adv. Model. Earth Syst.*, **13**, e2021MS002484, https://doi.org/10.1029/2021MS002484.

Zrnić, D. S., and Coauthors, 2007: Agile-beam phased array radar for weather observations. *Bull. Amer. Meteor. Soc.*, **88**, 1753–1766, https://doi.org/10.1175/BAMS-88-11-1753.

——, S. E. Koch, R. D. Palmer, M. E. Weber, K. D. Hondl, G. M. McFarquhar, and M. H. Jain, 2019: How an agile-beam polarimetric phased-array radar can add to the observing capabilities of the NWS. *Phased Array Radar Symp.*, Phoenix, AZ, Amer. Meteor. Soc., 2.3, https://ams.confex.com/ams/2019Annual/meetingapp.cgi/Paper/351777.